UC Santa Cruz
UC Santa Cruz Previously Published Works

Title

Operando leaching of pre-incorporated Al and mechanism in transition-metal hybrids on carbon substrates for enhanced charge storage

Authors

Guo, Wei
Yang, Feipeng
Yu, Chang
et al.

Peer reviewed

Operando leaching of pre-incorporated Al and mechanism in transition metal hybrids on carbon substrates for elaborately enhanced charge storage

Wei Guo[1,2,3], Feipeng Yang[2], Chang Yu[1,*], Yuanyang Xie[1], Jiuke Chen[4], Yisheng Liu[2], Yang Zhao[2], Juan Yang[6], Xuefei Feng[2], Shaofeng Li[1], Zhao Wang[1], Jinhe Yu[1], Kunlun Liu[1], Kun Qian[4], Mesfin Tsige[4], Qiuyu Zhang[3,*], Jinghua Guo[2,*], and Jieshan Qiu[1,5,*]

[1]State Key Lab of Fine Chemicals, School of Chemical Engineering, Liaoning Key Lab for Energy Materials and Chemical Engineering, Dalian University of Technology, Dalian 116024, China

[2]Advanced Light Source (ALS), Lawrence Berkeley National Laboratory, Berkeley, CA 94720, USA,

[3]School of Chemistry and Chemical Engineering, Northwestern Polytechnical University, Xi'an 710129, PR China

[4]Department of Polymer Science, The University of Akron, Akron, OH 44325, USA

[5]College of Chemical Engineering, Beijing University of Chemical Technology, Beijing 100029, China

[6]School of Chemical Engineering and Technology, Xi'an Jiaotong University, Xi'an 710049, China

*Correspondence and requests for materials should be addressed to C. Yu (chang.yu@dlut.edu.cn), Q. Zhang (qyzhang@nwpu.edu.cn), J. Guo (jguo@lbl.gov), or J. Qiu (jqiu@dlut.edu.cn, qiujs@mail.buct.edu.cn)

SUMMARY

Insufficient exposure and utilization of active sites often induces an inferior reactivity for transition metal-based two-dimension materials. In response, we for the first time propose a universal 'nano tailoring' strategy to incorporate abundant defects and active sites into low-crystallinity nanosheets by electrochemically leaching of Al species. With MnAl layered double hydroxides (LDH) as a representative example, potassium-birnessite MnO_2 (AK-MnO_2) with oxygen vacancies and abundant edge sites are successfully produced. The oxygen vacancies are evidenced to help optimize the electron-transfer and ion-adsorption capability. These integrated advantages endow the AK-MnO_2 with a high capacitance value of 239 F g^{-1} at 100 A g^{-1}. Further combined with soft X-ray absorption spectroscopy techniques, we unravel that the reducibility of M^{2+} in M^{2+}Al-LDH serves as the key descriptor for the reconstruction rate. This 'nano tailoring' strategy can provide some important implications and clues to manipulate 2D materials for efficient energy storage and conversion.

Keywords: dynamic leaching, structure reconstruction, intrinsic active species, carbon, high-rate energy storage

INTRODUCTION

With the development of social science and technology, the strong need of fast, sustainable and high-power energy storage systems have led to the quick development of supercacitors, which can be divided into two kinds: electric double layer capacitors (EDLCs) and pseudocapacitors (PCs).[1-2] When compared to EDLCs, the PCs are generally endowed with reversible surface/near-surface reactions to store more charges, thus demonstrating highly enhanced capacitive performance.[3-5] For configuring better PCs, rational modulation and optimization of reactive sites to activate the intrinsic properties of electrode materials are highly desired, serving as the key point for advancing energy storage.[6-8]

Generally, transition metal materials with intrinsic/extrinsic pseudocapacitive

properties are identified to be highly effective and indispensable for electrochemical energy storage (EES) because of their high theoretical capacitance, superior flexibility and excellent electronic properties.[9-11] Nevertheless, the inferior actual performances, which is far lower than the theoretical value, serving as the main barrier to the practical applications.[12-14] This is mainly caused by poor accessibility of active sites and largely restricted reaction dynamics. To solve these issues, developing new & effectively physical or chemical methods to simultaneously ameliorate the intrinsic redox reaction characteristics and surface microstructure properties are highly desired.

It is widely accepted that high-crystallinity materials generally suffer from the difficulties in expansion and extraction of lattice planes, thus leading to the hindered permeation and transport of electrolyte ions to some degre.[15] Besides, the highly ordered structure would be dynamically unfavourable for the sufficient reaction of redox species. In this regard, regulating the crystallinity of these type of materials may lead to the positive modulation of redox reaction dynamics. In extreme cases, it has been identified that transforming the crystalline structure into the low-crystallinity/amorphous one can introduce many internal disorders, grain boundaries and danling bonds, leading to an effective exposure of active sites, facilitated ions transport and promoted reactivity.[16-17] Besides, the *in-situ* introduced defects can produce many coordinately unsaturated and accessible sites, further enlarging active area for the optimization of redox dynamics.[18-21] These defects can also somehow modulate the electronic structure and surface chemistry, thereby promoting interfacial electronic transfer and mass transport.[22-25] With this information in mind, it is easy to be believed and anticipated that much hastened charge-storage process can be realized accordingly. For example, a previous result demonstrated that the amorphous $Ni(OH)_2$ delivered a capacity of about 20% and 60% higher than that of the crystalline α- and β-$Ni(OH)_2$, respectively.[26] The low-crystallinity FeOOH, derived from the crystalline α-Fe_2O_3 can demonstrate a exceptionally high capacitance value of 1066 F g^{-1}, superior to those of most Fe-based electrode materials.[27] Another tough issue for the configuration is the formation of the bulky structure in some cases, which leads to a

fairly long electron-transfer paths and relatively sluggish ion diffusion. Accordingly, many endeavors have been made to endow the tailor-made electrode materials with more surface and edge active sites, leading to an optimization of both capacitance and rate performance.[28-30] To sum up, holistic activation in terms of both crystalline engineering and nano-structure is desperately warranted for the promotion of the electrochemical performance.

Electrochemical configuration/modulation technique features the sound tunability toward the electronic structure, phase components and defective sites, attracting great attention in recent years in energy-related field.[31-33] Moreover, the low-energy-cost and time-saving characteristics render it a great potential for large-scale applications. It has been proved that the *in-situ* leaching of inactive species in the electrochemical enviroment and the correponding phase regulation can help produce the low-crystallinity and defects-enriched microstructure with tuned morphologies.[34-35] In this regard, the further progress requires the development of a universal methodology/strategy to tailor the generally adopted materials into highly active ones with modulated structures in terms of nano-/micro- and atom scale. To the best of our knowledge, aluminum, as a typical amphoteric metal element, displays a tendency and spontaneity to be dissolved in alkaline electrolytes, while it is thermodynamically unfavourable for transition metal elements. In addition, Al-based transition metal hybrids have a big familiy, such as double/triple/multiple oxides, hydroxides, sulfides and so on. Accordingly, it is expected that pre-incorporating of Al into the lattice of transition metal hybrids, followed by its *in-situ* leaching, can generate a series of advanced materials with promoted reactivity, which remains less concerns and requires more attention and detailed explorations.

Herein, a universal 'nano tailoring' strategy, *via* the *operando* leaching of pre-incorporated Al driven by electrochemical effect, is firstly proposed here for realizing holistic activation of transition metal hybrids. With MnAl layered double hydroxides (LDH) as a demonstration, the low-crystallinity potassium-birnessite MnO_2 (AK-MnO_2) can be produced quickly after the 'nano tailoring' process. With the help of soft XAS

(sXAS) technique, the structural evolution is finely tracked and decoupled. Interestingly, due to the irreversibly leaching of Al and the intercalation of K^+, the microstructure may undergo the emerging and releasing of internal strain, resulting in the positively tailored microstructure with enriched edge sites and oxygen vacancies (V_o). Also, density functional theory calculation demonstrates that the introduced oxygen vacancies would be capable of promoting charge transfer and facilitating the adsorption of electrolyte ions, leading to the optimized reaction kinetics for charge storage. As such, the as-formed AK-MnO$_2$ hybrids can deliver a high capacitance value of 356 F g^{-1} at 1 A g^{-1}, with a high retention rate up to 67% at a super-large current density of 100 A g^{-1}, indicative of a superior rate performance. More importantly, the universality of the 'nano tailoring' process to generate low-crystallinity nanosheets with enriched active sites is deeply verified and decoupled. We reveal that the leaching transformation is highly dependent on the reducibility of the adopted M^{2+}, which acts as a prominent factor for the reconstruction rate. It is believed that the unique and universal 'nano tailoring' strategy can stimulate broad interests and many inspirations of researchers to configure novel and highly efficient materials with positively tuned properties.

RESULTS AND DISCUSSION

Nano tailoring of LDH precursors and the tracking of dynamic microstructure.
As illustrated in **Figure 1**A, the 'nano tailoring' strategy involves with the M^{2+}Al-based binary hydroxides as the precursor, where the molecular breaking and reconstruction happens during the electrochemical-scanning process in alkaline media. As a typical example, during the 'nano tailoring' process, the MnAl-LDH would undergo the transformation into MnAl-based hydroxides, accompanied by partially leaching of Al, when soaked in alkaline electrolyte for a short time (2 min), yielding (Mn(Al)-OH) as the intermediate. Subsequently, it will be reconstructed into low-crystallinity birnessite-type MnO$_2$ with K^+ in the interlayer after CV cycling treatment, denoted by AK-MnO$_2$. The dynamic reconstruction is *ex-situ* tracked by scanning electron microscopy (SEM) images and the corresponding size distributions. As shown in **Figure 1**B-D, the large-

size LDH nanosheets are broken and reconstructed to a much smaller ones with a higher stacking density. The average size decreases from 726 nm for MnAl-LDH to 202 nm for Mn(Al)-OH hybrids, and finally to 55 nm for AK-MnO$_2$ hybrids (about 13 times decrease in size). Notably, the small and dense nanosheets would deliver more abundant active sites and feature numerous short-distance channels for fast charge transfer, thus beneficial for high-efficient charge storage.

The microstructure is further uncovered by the transmission electron microscope (TEM) images. As depicted in **Figure S1**A, the MnAl-LDH precursor displays the large size, and a lattice spacing of 0.26 nm corresponds to the (012) plane of LDH. For the Mn(Al)-OH, the broken structure with *in-situ* formed numerous holes can be observed and the lattice spacing of 0.33 nm corresponds to (100) plane of Mn(OH)$_2$ (**Figure S1**B). Impressively, the well-tailored AK-MnO$_2$ with densely stacked and ultra-small nanosheet microstructure (**Figure 1**E), displays a low crystallinity, as shown in the HR-TEM image (**Figure 1**F). It is further identified by the result of selected electron diffraction (SAED), where no lattice patterns can be detected (**Figure 1**F), indicative of the generation of lattice distortion and randomly stacked internal construction. Furthermore, as presented by the high-angle annular dark-field scanning TEM (HAADF-STEM) images and the corresponding elemental maps, the Mn, O, K elements are uniformly distributed on the surface of AK-MnO$_2$ (**Figure 1**E). Also, we have carried out atomic force microscopy (AFM) characterization to better study the morphology of the AK-MnO$_2$. As shown in **Figure S2**, the ultrathin and wrinkled nanosheet morphology with a thickness of about 7.7 nm is presented. Besides, the AK-MnO$_2$ demonstrates the highly increased surface area (157 m^2 g^{-1}) as well as more abundant pore structure (**Figure S3**), when compared with that of the MnAl-LDH (58 m^2 g^{-1}). The enlarged surface area, enabled by the novel 'nano tailoring' process, can help access to more electrolyte ions at a given time and shorten the transport distance, thus accounting for the enhanced charge storage.

The 'nano tailoring' process of the MnAl-LDH is further decoupled by X-ray diffraction (XRD) patterns (**Figure S4**). Notably, the intensive peaks located at 26.4,

6

43.1, 54.6 and 77.6° can be indexed to the characteristic peaks of carbon paper (CP). For the MnAl-LDH hybrids, the peaks at 10.1, 20.2, 33.1, 36.4 and 58.8° can be indexed to the (003), (006), (012), (015), (110) planes of LDH phase, respectively. Explicitly, for the Mn(Al)-OH hybrids, the peaks at 18.8, 31.6, 36.8, 49.9 and 59.5 can be indexed to (001), (100), (101), (102), (111) diffraction planes of $Mn(OH)_2$ (JCPDS Card no. 18-0787), respectively, indicative of the phase transformation from MnAl-LDH to Al-doped $Mn(OH)_2$ phase. However, for the AK-MnO_2, it displays only one significant peak at about 12.7°, as well as an indiscernible wide band in the range of 35 to 40°. It implies the low-crystallinity/amorphous features for the [MnO_6] octahedra laminate.[36-37] Notably, an increase of interlayer spacing from Mn(Al)-OH (d-spacing: 4.7 Å) to AK-MnO_2 (d-spacing: 7.0 Å) can be attributed to a certain amount of K^+-intercalated into the interlayer. To further confirm the existed species, Raman measurements are carried out. For the AK-MnO_2 hybrids, the characteristic peaks at 265, 317, 396, 469, 578 and 654 cm^{-1} are matched with those of birnessite-type MnO_2 with a little shift (**Figure 1**G), attributed to the varied ion radius between K^+ and Na^+.[38] And the intense peaks at 1350 cm^{-1} and 1580 cm^{-1} can be indexed to the D- and G- bands of CP. Moreover, Raman maps are recorded in the green, orange and pink regions (as marked in **Figure 1**G), where the uniform distribution for the signals of CP (orange and pink) and AK-MnO_2 (green) is presented in the maps (**Figure 1**H), indicative of the intimate interaction between them.

sXAS and theoretical calculation decoupling the fine structure. Moreover, sXAS technique is used to decouple the fine structure of the as-formed hybrids and understand the dynamic phase reconstruction process. The mechanism of sXAS is illustrated and displayed in **Figure 2**A. To be specific, the incident X-ray can induce the transition of electrons to the excited state and produce a core hole *in situ*. Then the decay of the excited-state electrons to the same core hole would generate elastic energy to be detected.[39] sXAS is available to probe the chemical conditions of materials from surface to bulk. And the generated signals can be divided into total electron yield (TEY, depth:

2-5 nm) and total fluorescence yield (TFY, depth: about 50 nm).[40] The Mn L-edge soft XAS spectra are shown in **Figure 2**B. It is worth noting that the typical peaks at 638.8, 640.2 and 641.6 eV can be assigned to Mn^{2+}, Mn^{3+} and Mn^{4+}, respectively, while the peak intensity is generally used to identify the relative content.[41] Clearly, for the MnAl-LDH, the peak at 638.8 eV is much more intensive than the others, implying that the Mn primarily exists in +2 status. When compared to the MnAl-LDH, the Mn(Al)-OH hybrids are also dominated by Mn^{2+}, despite the slight increase in peak intensity of Mn^{3+}. Interestingly, the Mn^{4+} ions are dominated for the as-formed AK-MnO_2, where a certain amount of Mn^{3+} are still remained. It is noteworthy that the charge compensation can be realized by the intercalation of K^+, which would be described below in detail. Moreover, compared with the 30-cycled sample (AK-MnO_2), no further obvious changes in Mn L-edge are found after 50 cycles, implying that the stable status can be attained after 30 cycles. These results finely correspond to the Mn 2p and Mn 3s XPS results (**Figure S5**). To gain a more complete picture on the reconstruction process, the O K-edge characterization is conducted (**Figure 2**C). The pre-edge region (below 533 eV) and broad band region (over 533 eV) can be attributed to the transition of O 1s to Mn 3d and O 2p hybrid-state orbital, and O 1s to Mn 4sp and O 2p hybrid-state orbital, respectively. Generally speaking, the positive shift of the broad band can indicate the increase in Mn valence.[42] Compared to the MnAl-LDH, there is no detectable shift of the broad band detected for the Mn(Al)-OH, indicative of the unobvious oxidation of Mn species. Nevertheless, the significantly positive shift can be detected for the 30-cycled sample (AK-MnO_2), indicative of the oxidation of Mn species to a great degree. The 50-cycled sample demonstrates no more shift when compared with that of the AK-MnO_2, indicative of the complete transformation after 30 electrochemical cycles, well consistent with the results we mentioned above.

For the C K-edge spectra (**Figure S6**), the two new peaks at 299 eV and 302 eV, which corresponds to the characteristic peaks of K L_3 and L_2-edge,[43] emerge for 30- and 50-cycled electrodes, indicative of the intercalation of K^+. This is further proved by the presence of the intense K 2p peak signals for AK-MnO_2 (**Figure S7**A). On top of that,

the drastic reconstruction process enables the formation of internal defects to a great degree, which is studied and analyzed by the depth spectra of O 1s (**Figure 2**D). The peaks located at 530, 531.7 and 533 eV can be finely detected, corresponding to the bonding of metal-oxygen, oxygen vacancy and physic-/chemical-adsorbed O, respectively.[44-45] Impressively, the intensive peak at 531.7 eV implies the significant amount of oxygen vacancies (V_o) for the as-formed AK-MnO$_2$ hybrids. Then, the HAADF-STEM characterization is carried out *via* spherical aberration corrected TEM (AC-TEM) technique to visualize the oxygen vacancies of the AK-MnO$_2$. As shown in **Figure S8**, the AK-MnO$_2$ displays the ultra-thin and wrinkled nanosheet morphology. Notably, many created defective sites are distributed at the edge of the nanosheets (**Figure 2E**, **Figure S8**). Besides, according to the intensity profile along the rectangular region, the missed O atom and O defect are observed. For comparison, the high-crystalline MnO$_2$ (HC-MnO$_2$) was also fabricated, please refer to **Figure S9** for details.

The dynamic leaching of Al is tracked by Al *K*-edge spectra, acquired *via* TFY and TEY scan models. As shown in **Figure S6**B, the Al K-edge signal in the sXAS/TEY spectrum of the Mn(Al)-OH hybrids demonstrates a decrease when compared to that of the MnAl-LDH, then disappears completely for the AK-MnO$_2$ hybrids, indicative of the gradual leaching of Al from the microstructure. Likewise, no obvious Al *K*-edge signal is demonstrated for the sXAS/TFY scan of AK-MnO$_2$ (**Figure 2**F), implying that Al has been leached completely. Furthermore, Al 2p spectra characterization is further carried out, where a finely consistent result is detected (**Figure S7**B). To evaluate the key factors of the 'nano tailoring' process, a series of control experiments are conducted. On one hand, to understand the effect of Al, we also prepare Mn(OH)$_x$ (denoted as Mn-OH) *via* the same process like that of MnAl-LDH but without the addition of Al source. It well accords with the phase structure of Mn(OH)$_2$ (**Figure S4**). Interestingly, when treated by same 'nano tailoring' process like that of the MnAl-LDH, the Mn-OH cannot be finely and fast reconstructed into the small-size nanosheets, manifesting that the deep reconstruction reaction is unfavorable or relatively poor in dynamics. For more details,

please refer to **Figure S10-13**. On the other hand, the effect of electrochemical CV scanning treatment is also discussed. For comparison, the MnAl-LDH was just immersed in 6 M KOH electrolyte without the CV scanning treatment, and the reaction time is kept consistent with that of the 'nano tailoring' process. However, the insufficient oxidation and reconstruction process is detected (**Figure S14**), demonstrating that the CV scanning treatment serves as the vital factor to efficiently boost the structure evolution to a great degree. As mentioned above, it can be concluded that Al-leaching can make sure the formation of meta-stable intermediates to initiate the reconstruction process, where the deep oxidation and reconstruction is further facilitated and finished by the electrochemical CV scanning treatment.

To understand the underlying effects of oxygen vacancies in the microstructure of the AK-MnO$_2$ hybrids, density function theory (DFT) calculation is carried out. The potassium-birnessite MnO$_2$ without or with oxygen vacancies are used as the models for the calculations (**Figure 2**G and I). The lattice parameters of the used potassium-birnessite MnO$_2$ were listed in **Table S1**. For the potassium-birnessite MnO$_2$ without oxygen vacancies, the total density of state (TDOS) and partial density of state (PDOS) at the Fermi level (E_F) set at 0 eV display the detectable band gap, indicative of the semiconductor properties as illustrated in **Figure 2**H. While with V$_o$, the continuous TDOS and PDOS (**Figure 2**J) near E_F can be detected, indicative of the efficient electron transfer and highly improved electrical conductivity.[46]

Moreover, the adsorption of sodium ion was decoupled. The optimized adsorption structures of hydrated sodium ion onto the surface of potassium-birnessite MnO$_2$ without or with oxygen vacancies are shown in **Figure 2**K-L. When with oxygen vacancies, the hydrated sodium ion adsorption energy over the materials is -4.60 eV, which is lower than that of the potassium-birnessite MnO$_2$ without oxygen vacancies (-4.20 eV). Thus, due to the existence of considerable amount of oxygen vacancies, sodium ion adsorption would be energetically favorable on the surface, responsible for boosting the surface/interface reaction kinetics.

The universality of the 'nano tailoring' process and the involved two distinct mechanisms. To investigate and explore the universality of the 'nano tailoring' strategy, other extensively studied LDH, such as CoAl-LDH and NiAl-LDH, are also prepared following the similar electrodeposition method and then treated by the 'nano tailoring' process. For the as-formed CoAl-LDH, the large nanosheets microstructure with the average size of about 325 nm can be observed (**Figure 3**A, C). Subsequently, the 'nano tailoring' process is carried out similar to that of the MnAl-LDH, triggering the fast Al leaching and structure reconstruction (**Figure S15-16**). It is interesting that the derived hybrids deliver the nanosheets structure with an average size of about 50 nm with a little aggregation (**Figure 3**B, C and **Figure S16**C, D), displaying about 7 times decrease in size when compared with that of the pristine CoAl-LDH. The small nanosheet clusters with short electron transfer path and abundant transfer channels feature a potential to robustly boost charge-storage efficiency for fast and efficient energy storage. Moreover, as revealed by the HAADF-STEM images and the corresponding elemental maps, Co and O elements are uniformly distributed on the as-formed hybrids (**Figure 3**D). Similar to that of the AK-MnO$_2$, the nanosheets are also low crystallinity (**Figure 3**E), due to the rapidly dynamic reconstruction-induced the formation of unsaturated sites and defects, thus contributing to the following high reactivity.

To gain a more clear understanding on the microstructure, the evolution of the phase components during the reconstruction process is tracked by XRD patterns in detail. As the 'nano tailoring' process goes on, the CoAl-LDH is transformed to CoOOH phase (JCPDS Card no. 07-0169) with a low crystallinity after 50 electrochemical cycles (**Figure S17**A). After 200 cycles, the crystallinity further decreases and only the peak corresponding to the interlayer spacing can be detected, indicative of the low-crystallinity/amorphous features in the [CoO$_6$] laminate, thus corresponding to the HR-TEM results (**Figure 3**E). The finally derived low-crystallinity CoOOH structure is thus labeled as A-CoOOH.

The dynamic reconstruction process is further studied by the sXAS spectra. The Co

L-edge spectrum of the CoAl-LDH displays the typical peaks a and b that can be indexed to the Co^{2+}, indicative of the Co^{2+}-dominated feature (**Figure 3**F). However, after 50 cycles, the intensity of two peaks decreases to a great degree while a new intensive peak emerges, denoted as peak c that is corresponding to Co^{3+}, indicative of the significant oxidization of Co^{2+} to Co^{3+}.[47] After 200 cycles (A-CoOOH), the peaks a and b completely disappear while the peak c keeps a high intensity, indicative of the deep evolution and transformation from Co^{2+} to Co^{3+}. This is also confirmed by the Co 2p XPS spectra (**Figure S17**B), which is displayed and discussed in the supporting information. For the O *K*-edge of the CoAl-LDH, the pre-peak at about 531.1 eV can be assigned to the hybridization of Co 3p to O 2p.[48] After 50 and 200 cycles, the peak intensity displays a significant increase while the position demonstrates a negative shift (**Figure 3**G), indicative of the intensified and modulated Co-O hybridization during the evolution process. Moreover, to further understand the key role of Al, a control experiment is carried out. To be specific, $Co(OH)_2$ with nanosheets-shaped structure is formed by the similar electrodeposition process without Al source. Then it is treated by the same process like the CoAl-LDH. However, the nanosheets are transformed into the bulky structure instead of small-sized nanosheets (**Figure S18**), vividly confirming that the *in-situ* leaching of Al is of great importance for the success of the 'nano tailoring' process.

Some similar but not exactly the same results are witnessed for the NiAl-LDH. The NiAl-LDH fabricated through electrodeposition also displays the uniform nanosheets microstructure with an average size of about 202 nm (**Figure 3**H, J). Subsequently, the 'nano tailoring' process is proceeded and the corresponding microstructure evolution is further tracked and analyzed. Notably, the morphology displays the sluggish change, and the significant structure destruction into the small nanosheets (with a size of about 77 nm) is detected after 400 cycles, (**Figure 3**I, J and **Figure S19**A-B). Moreover, as demonstrated in the HAADF-STEM image and elemental mapping images, Ni, and O elements are uniformly distributed in the 400-cycled NiAl-LDH, while the signal of Al is weakened a lot when compared to that of the pristine NiAl-LDH (**Figure 3**K and

Figure S20). And as demonstrated in the HR-TEM image (**Figure 3**L) and XRD results (**Figure S19**C), the 400-cycled NiAl-LDH also delivers the low-crystallinity feature like the AK-MnO$_2$ and A-CoOOH, thus denoted as A-NiAl-LDH. Somewhat surprisingly, based on the SEM/Energy Dispersive X-Ray Spectroscopy (EDS) and depth XPS results, considerable amount of Al species are still present on the surface and sub-surface after the 'nano tailoring' process (**Figure S19**D-F).

In order to further understand the bonding information and electronic structure, the reconstruction of the NiAl-LDH during the 'nano tailoring' process is studied and decoupled by the sXAS spectra (TEY mode). The Ni *L*-edge spectrum of the NiAl-LDH is exactly comparable to that of the Ni(OH)$_2$ reference sample, implying that Ni^{2+} is dominated in the microstructure (**Figure 3**M).[49] After 400 and 800 cycles, the spectra display no appreciable changes when compared to that of the pristine NiAl-LDH. With this information in mind, it can be concluded that there is no apparent increase for the valence state of Ni during the 'nano tailoring' process. Furthermore, the O *K*-edge spectra of the as-formed hybrids are also examined and analyzed (**Figure 3**N). The pre-peak of the O *K*-edge can be attributed to the hybridization of Ni 3d and O 2p.[50] Compared to the pristine NiAl-LDH, a positive shift of the pre-peak can be detected after 400 and 800 cycles, which becomes closer to the Ni(OH)$_2$ reference sample. It implies the tuned interaction between Ni and O during the 'nano tailoring' process, which is triggered by the irreversible Al leaching and surface electronic structure modulation.

The C *K*-edge spectra of the NiAl-LDH and that after 400 cycles (A-NiAl-LDH), as well as the CoAl-LDH and that after 200 cycles (A-CoOOH) are further examined. It is noteworthy that the significant peaks at around 300 eV for the A-CoOOH can be observed, corresponding to the typical peaks of K *L$_3$*- and *L$_2$*- edge, as we mentioned before. It indicates that the intercalation of K$^+$ happens during the 'nano tailoring' process for the CoAl-LDH, which is similar to that of the MnAl-LDH. However, on the other hand, the typical peaks of K *L*-edge cannot be detected for the A-NiAl-LDH (**Figure S21**), implying that K$^+$ is unfavorable or sluggish in dynamics to intercalate

into microstructure of the NiAl-LDH during the 'nano tailoring' process.

As mentioned above, some underlying principles are surely followed for the 'nano tailoring' process, which is uncovered and discussed here. In general, the reducibility of M^{2+} in LDH acts as a vital factor for the 'nano tailoring' process, and the reconstruction mainly involves two distinct types, as illustrated in **Figure 3**O: (1) oxidization-boosting type (such as Mn^{2+}, Co^{2+}); (2) non-oxidization type (such as Ni^{2+}). For the oxidization-boosting type, M^{2+} features the metastable characteristics with a strong oxidation tendency. Accordingly, the as-generated strong internal strain would result in the mismatched electronic construction, thus inducing the formation of unsaturated sites and numerous defects for ultra-fast Al leaching. The dramatic Al leaching results in the significant loss of positive charges, thus attracting the irreversible intercalation of the univalent charge carriers (K^+ ions) as the compensation charges.[51-52] In the meantime, K^+ may serve as the electron donors and bond with O atom to some extent, thus weakening the bonding of M-O and producing some oxygen vacancies.[53] Finally, the phase evolution process would be accelerated. For the second type, M^{2+} is thermodynamically stable and unfavorable to be oxidized, demonstrating the well-matched electronic construction and a robust interactive bonding. Due to the lack of the strong internal strain effects, the phase evolution is highly restricted and sluggish in dynamics. In this case, given that Al leaching displays a slow rate, the partially removing of interlayer anions would be capable enough to well maintain the charge balance.[54] Therefore, a prodigious energy barrier would be required for K^+ intercalation, which would hardly occur. To sum up, it is exciting to note that the 'nano tailoring' process is universal for the top-down configuration of low-crystallinity and small-sized electrode materials with structural defects though the different leaching process is presented, possessing great prospects for serving energy and catalysis fields.

Characterization and evaluation of the electrochemical performance. The electrochemical performance of the as-made hybrids are evaluated. Impressively, for the AK-MnO$_2$ hybrids, even at a super-high scan rate of 1 V s^{-1}, no significant

deformation for CV curves can be detected (**Figure 4**A), indicative of the superior rate performance. The charge-storage capability in terms of surface/interface reaction dynamics is further decoupled by the following equation:

$i=av^b$

Or written as:

$\log(i)=b\log(v)+\log(a)$ (a, b are constant)

Here, b value can be applied to determine surface reaction-dominated contribution (when b value is near 1.0) and diffusion-dominated contribution (when b value is near 0.5). It is found that the b value for the AK-MnO$_2$ is greater than 0.8 at different voltages, and this value is greater than 0.9 at the range of 0-0.72 V, indicative of the surface reaction-dominated charge-storage process (**Figure 4**B). Subsequently, the capacitive contribution is evaluated based on the CV curves, which is explained and analyzed in **Figure S22**. Accordingly, it can be found that the capacitive contribution can reach 84% at 2 mV s^{-1}, 85% at 5 mV s^{-1}, 87% at 10 mV s^{-1}, 91% at 20 mV s^{-1} and up to 94% at 30 mV s^{-1} (**Figure 4**C and **Figure S22**), indicative of a surface reaction-dependent charge storage process, and responsible for a high rate performance and stability. Subsequently, the EIS measurements are conducted. Generally speaking, the solution resistance (R_s, obtained by the X-intercept of the Nyquist plots) is used to identify the internal barrier and ion response capability, while the charge-transfer resistance (R_{ct}, obtained by the diameter of the semicircle of the Nyquist plots) is used to evaluate the charge-delivery capability at the electrode/electrolyte interface. The Nyquist plots are displayed in **Figure S23**. It is found that the AK-MnO$_2$ exhibits the significantly reduced R_{ct} and R_s value when compared with the counterparts. And the IR drop value is 69 mV at 50 A g^{-1}, and only 146 mV even at a super-large current density of 100 A g^{-1} (**Figure 4**D), further indicative of a lower internal resistance. The Coulombic efficiency is 98% at 1 A g^{-1} and can reach over 98% at different current densities, manifesting the highly reversible charge-storage process, with a superior stability. Therefore, the AK-MnO$_2$ is capable of concurrently realizing a high Coulombic efficiency and low IR drop, superior to other electrodes to some degree (**Figure S24-25**). The optimal mass-

transport and charge-transfer kinetics can be well accomplished by engineering the highly defective, active sites-enriched microstructure. The AK-MnO$_2$ electrode delivers a high capacitance value of 356 F g^{-1} at 1 A g^{-1}, with an ultra-high retention rate of 67% at 100 A g^{-1}, indicative of a very sound rate performance, outperforming the Mn(Al)-OH, MnAl-LDH, HC-MnO$_2$ and 30-cycled Mn-OH electrodes to a great degree (**Figure 4**E, **Figure S25**). That is to say, thanks to the 'nano tailoring' process, the microstructure is endowed with the *in-situ* incorporated oxygen vacancies, as well as the abundant accessible area or favorable active edge sites, eventually promoting its mass transport and charge transfer process for efficient energy storage. In addition, a sound retention rate of 85% is realized for the AK-MnO$_2$ after 5000 cycles at 6 A g^{-1} (**Figure 4**F, **Figure S26**), indicative of the highly stability. These decent capacitive properties are all at the front rank among previously reported MnO$_2$-based electrodes (**Table S2**). Considering the mass loss after 'nano tailoring' process, the electrodes with same mass loading were fabricated by varying the electrodeposition time of the precursor and their performances were further compared. As shown in **Figure S27**, the capacitance performance of the as-formed AK-MnO$_2$ is much superior to the counterparts. On the other hand, thanks to the 'nano tailoring' process, the superior charge storage capability can be also realized for A-CoOOH and A-NiAl-LDH, please refer to **Figure S28-29** for details. Therefore, with the positive effects of 'nano tailoring' process, the sharply strengthened charge storage capability is gratifyingly reached. It is expected that these findings would give more possibilities in energy field and help with the generation of more insightful inspirations and attempts. Also, to enable substantial achievements in methodology, it would be highly appreciated to *operando* track the surface/interface interaction, coordination information as well as the spatially charge distribution. And it is highly recommended to develop time-saving, controllable and low-cost configuration methods for the upcoming green & sustainable energy system.

Conclusion

In summary, a universal 'nano tailoring' strategy is presented here to robustly convert

the transition metal hybrids into low-crystallinity, active edge sites and vacancies-enriched hybrids, where the involved phase-evolution rule is unveiled and decoupled with the help of the sXAS technique. As the representative sample, the 'nano tailoring' process triggers the transformation of the MnAl-LDH into the low-crystallinity AK-MnO$_2$, accompanied by the *in-situ* incorporation of abundant active sites and oxygen vacancies. Furthermore, as demonstrated by the DFT calculation results, the oxygen vacancies in the microstructure can not only help facilitate the electron transfer process, but also boost the adsorption of hydrated Na$^+$ for the enhanced reaction dynamics. As such, the as-formed AK-MnO$_2$ hybrids can deliver a high capacitance value of 356 F g^{-1} with an ultra-high retention rate of 67% at a super-large current density of 100 A g^{-1}, indicative of a very superior rate performance. More importantly, the 'nano tailoring' process features the sound universality that can also *in-situ* transform the NiAl-LDH and CoAl-LDH into the transition metal hybrids with low-crystallinity and highly active microstructures. Furthermore, we propose a principle of the 'nano tailoring' process and further divide it into two main branches based on the reducibility of M^{2+} in the M^{2+}Al-LDH: (i) oxidization-boosting type and (ii) non-oxidization type, where the reaction rate and structural evolution process features a substantial difference. It is expected that this 'nano tailoring' strategy would provide and spur many opportunities and ideas for configuring kinetically favorable nanomaterials, serving as a good model and reference for the development of materials adopted in energy- and catalysis-related fields.

EXPERIMENTAL PROCEDURES

Resource Availability

Lead Contact

Further information and requests for resources and reagents should be directed to and will be fulfilled by the Lead Contact, Jieshan Qiu (e-mail: jqiu@dlut.edu.cn).

Materials Availability

All chemicals were purchased from commercial suppliers and used directly without further purification: $Mn(NO_3)_2$ aqueous solution, $Al(NO_3)_3 \cdot 9H_2O$ and $Ni(NO_3)_2 \cdot 6H_2O$ are purchased from Xilong Scientific Co., Ltd.; $Co(NO_3)_2 \cdot 6H_2O$, $KMnO_4$, KOH and Na_2SO_4 are purchased from Tianjin Kemiou Chemical Reagent Co., Ltd.; the carbon fiber is purchased from Shanghai Hesen Electric Co., Ltd..

Data and Code Availability

This study did not generate/analyze datasets/code.

Fabrication of the MnAl-LDH, Mn(Al)-OH, and AK-MnO₂

The MnAl-LDH nanosheets were fabricated by the simple electrodeposition method. Firstly, CP (2×3.3 cm^2) was treated in 80 mL of concentrated nitric acid for 24 h to form the hydrophilic surface. After that, 0.6 mmol $Mn(NO_3)_2$, 0.4 mmol $Al(NO_3)_3$ were dissolved in 50 mL of deionized water under continuous stirring for 5 min, forming the light pink, transparent solution for electrodeposition. Then the pre-treated CP, saturated calomel electrode (SCE) and Pt plate (2×2 cm^2) were used as working electrode, reference electrode and counter electrode, respectively. The electrodeposition process was carried out on the CHI760D electrochemical workstation at a voltage of -1.5 V for 10 min, yielding light pink MnAl-LDH on CP. Next, the as-formed MnAl-LDH hybrids were soaked in 6 M KOH electrolyte for 2 min, yielding Mn(Al)-OH. Then, it was further cycled by a cyclic voltammetry technique with a voltage range of 0-0.6 V for 30 cycles, yielding AK-MnO₂ hybrids.

Fabrication of the Mn-OH

In comparison, the Mn-OH hybrids were formed by the similar electrodeposition process without the addition of Al source. The as-formed hybrids were washed by water and ethanol thoroughly, and dried at 60 °C for 2 h.

18

Fabrication of the HC-MnO₂

For fabrication of the HC-MnO₂, the pre-treated CP (2×3.3 cm^2) was immersed into the 40 mL aqueous solution containing 0.316 g KMnO₄. After being treated at 180 °C for 3 h in Teflon-lined autoclave, the HC-MnO₂ was formed. It was washed by water and ethanol thoroughly, and dried at 60 °C for 2 h.

Computational methods

The calculations, based on density function theory (DFT), were carried out by the CASTEP module in Materials Studio[55] (version 8.0, Accerly Corporation). The electron-ion interaction was described by Vanderbilt-type ultrasoft pseudopotentials (USPP) and the exchange-correlation function was treated using the generalized gradient approximation (GGA) of Perdew et al. as parameterized by Perdew-Burk-Ernzerhof (GGA-PBE) and with spin-polarized consideration.[56-57] For the present study, the GGA+U calculations with an empirical Coulomb repulsion term U value of 3.9 eV was employed for the d-like states of Mn atoms.[58] The energy cut-off of 520 eV was set for the plane-wave basis set and a $3\times8\times3$ net was used with the Brillouin zone sampling scheme of Monkhorst-Pack grid.[59] For highly precise results, self-consistent field (SCF) tolerance was 1.0×10^{-6} eV/atom.

Firstly, the geometrical optimization was performed and the convergence was defined as ultrafine tolerance with 5×10^{-6} eV atom^{-1} of the difference of total energy, 0.01eV Å^{-1} of maximum force, 0.02 GPa of maximum stress, and 5×10^{-4} Å maximum atomic displacement. After the optimization of the unit cells, the calculations of single point energy were performed and the total density of state (TDOS) and partial density of state (PDOS) of potassium-birnessite MnO₂ with and without oxygen vacancies were obtained.

For the calculations of adsorption energy, since the (001) facet is exposed naturally and is more stable with lower surface energy than the dominant (110) facets,[60] the (001) facet was cleaved and slab models with a 15 Å vacuum gap that are perpendicular to the surface were built. The Brillouin zone sampling was restricted to $3\times4\times1$ k-points

due to the larger size of the unit cell. After geometrical optimization of the slab, the hydrated sodium ion was added to the surface and the subsequent optimizations and calculations of single point energy were performed with fixed size of the unit cell because the introduction of ion did not significantly change the size and shape of the cell. The hydrated sodium ion was optimized in a $15 \times 15 \times 15$ Å^3 cubic box with the Γ-point and the same stopping criterion.

The adsorption energy (E_{ads}) of the hydrated sodium ion on the surface was computed from three pair given by:

$$E_{\text{ads}} = E_{(\text{H}_2\text{O/Na}^+\text{-KMnO}_2)} - (E_{\text{KMnO}_2} + E_{\text{H}_2\text{O/Na}^+})$$

where $E_{\text{H}_2\text{O/Na}^+\text{-KMnO}_2}$ is the total energy of the hydrated sodium ion adsorbed onto the (001) surface at hollow site, E_{KMnO_2} is the energy of the potassium-birnessite MnO_2 slab, and $E_{\text{H}_2\text{O/Na}^+}$ is the energy of the hydrated sodium ion.

SUPPLEMENTAL INFORMATION

Supplemental Information includes Supplemental Experimental Procedures, 29 figures and 2 tables.

ACKNOWLEDGMENTS

AUTHOR CONTRIBUTIONS

C. Yu, Q. Zhang, J. Guo and J. Qiu supervised the study. W. Guo and C. Yu designed the research. W. Guo carried out materials fabrication and most of the characterization.

C. Yu, Q. Zhang, J. Guo, and J. Qiu provided constructive advice for experiments. W. Guo, F. Yang, Y. Liu, Y. Zhao, X. Feng carried out the soft X-ray measurements. J. Chen, K. Qian, M. Tsige carried out DFT calculations. W. Guo, Y. Xie, J. Yu, K. Liu performed electrochemical measurements. J. Yang, S. Li, Z. Wang performed the TEM measurements. All authors discussed the results and commented on the manuscript.

DECLARATION OF INTERESTS

The authors declare no conflicts of interest.

Figure 1. A brief introduction of 'nano tailoring' strategy and its application for configuring low-crystallinity AK-MnO₂ hybrids. A, Schematic illustrations of the 'nano tailoring' strategy for formation of low-crystallinity hydroxides/oxides. Purple, pink, orange, green, blue, gray balls correspond to O, H, Mn (Co, Ni…), Al, K, N atoms, respectively. B-D, SEM images and the corresponding size distribution of (B) MnAl-LDH, (C) Mn(Al)-OH and (D) AK-MnO₂ nanosheets. E, TEM image and the corresponding elemental mapping images of AK-MnO₂ nanosheets. F, HR-TEM image of AK-MnO₂ nanosheets and the corresponding SAED pattern. G, H, Raman spectrum (G) and the corresponding mapping images (H) of AK-MnO₂ hybrids.

Figure 2. Fine structure characterization and theoretical calculation analysis. A, Schematic illustration of soft XAS mechanism and its two types of modes with different probe depth (referred to ref. [61-62]). B, C, TEY scans: Mn L-edge (B), O K-edge (C) of the MnAl-LDH, Mn(Al)-OH and 30-cycled (AK-MnO₂) and 50-cycled hybrids. D, O 1s spectra of the AK-MnO₂ hybrids. E, HAADF-STEM image of the AK-MnO₂, and the intensity profile along the selected rectangular regions, which suggests the missed/defective O atoms on the surface. F, TFY scan for Al K-edge of the MnAl-LDH and AK-MnO₂ hybrids. G, H, Molecular structure of the pure potassium-birnessite MnO₂ (G) and the corresponding DOS curves (H). I, J, Molecular structure of the potassium-birnessite MnO₂ with oxygen vacancies (I) and the corresponding DOS

curves (J). K, L, Schematic adsorption models for hydrated sodium ion on the surface of potassium-birnessite MnO_2 without (K) and with (L) oxygen vacancies.

Figure 3. The application of the 'nano tailoring' strategy to configure Ni- and Co-based low-crystallinity nanosheets. A, B, SEM images of (A) the CoAl-LDH and (B) the 200-cycled hybrids (A-CoOOH). C, Size distribution of the CoAl-LDH and A-CoOOH hybrids. D, HAADF-STEM image of the A-CoOOH and the corresponding EDS maps (*K*-edge). E, HR-TEM image of the A-CoOOH hybrids. F, G, Soft XAS spectra: Co *L*-edge (F) and O *K*-edge (G) spectra of the CoAl-LDH and the 50- and 200-cycled hybrids. H, I, SEM images of (H) the NiAl-LDH and (I) the 400-cycled hybrids (A-NiAl-LDH). J, Size distribution of the NiAl-LDH and A-NiAl-LDH hybrids. K, HAADF-STEM image of the A-NiAl-LDH and the corresponding EDS maps (*K*-edge). L, HR-TEM image of the A-NiAl-LDH hybrids. M, N, Soft XAS spectra: Ni *L*-edge (M) and O *K*-edge (N) spectra of the NiAl-LDH and that after 400 and 800 cycles. O, Schematic illustrations of the underlying principle of the 'nano tailoring' process.

Figure 4. Electrochemical performance and comparison of the hybrids. A, CV curves of the AK-MnO_2 hybrids at different scan rates. B, b values of the AK-MnO_2 at different voltages. Inset is the logarithm of current densities versus logarithm of scan rates for the AK-MnO_2 electrode. C, Capacitive contributions of the AK-MnO_2 at different scan rates. D, GCD curves of the AK-MnO_2. E, Specific capacitance of the MnAl-LDH, Mn(Al)-OH, 30-cycled Mn-OH and AK-MnO_2 at different current densities. F, Cycle performance of the AK-MnO_2 hybrids at 6 A g^{-1}.

REFERENCES

1. Simon, P., and Gogotsi, Y. (2020). Perspectives for electrochemical capacitors and related devices. Nat. Mater. *19*, 1151-1163.
2. Noori, A., El-Kady, M.F., Rahmanifar, M.S., Kaner, R.B., and Mousavi, M.F. (2019). Towards establishing standard performance metrics for batteries, supercapacitors and beyond. Chem. Soc. Rev. *48*, 1272-1341.
3. Salanne, M., Rotenberg, B., Naoi, K., Kaneko, K., Taberna, P.L., Grey, C.P., Dunn,

B., and Simon, P. (2016). Efficient storage mechanisms for building better supercapacitors. Nat. Energy *1*, 16070.

4. Nakhanivej, P., Yu, X., Park, S.K., Kim, S., Hong, J.Y., Kim, H.J., Lee, W., Hwang, J.Y., Yang, J.E., Wolverton, C., *et al.* (2019). Revealing molecular-level surface redox sites of controllably oxidized black phosphorus nanosheets. Nat. Mater. *18*, 156-162.

5. Guo, W., Yu, C., Li, S.F., and Qiu, J.S. (2021). Toward commercial-level mass-loading electrodes for supercapacitors: opportunities, challenges and perspectives. Energy Environ. Sci. *14*, 576-601.

6. Xia, Y., Mathis, T.S., Zhao, M.Q., Anasori, B., Dang, A., Zhou, Z., Cho, H., Gogotsi, Y., and Yang, S. (2018). Thickness-independent capacitance of vertically aligned liquid-crystalline MXenes. Nature *557*, 409-412.

7. Guo, W., Yu, C., Li, S.F., Wang, Z., Yu, J.H., Huang, H.W., and Qiu, J.S. (2019). Strategies and insights towards the intrinsic capacitive properties of MnO_2 for supercapacitors: challenges and perspectives. Nano Energy *57*, 459-472.

8. Choi, C., Ashby, D.S., Butts, D.M., DeBlock, R.H., Wei, Q., Lau, J., and Dunn, B. (2020). Achieving high energy density and high power density with pseudocapacitive materials. Nat. Rev. Mater. *5*, 5-19.

9. Tan, C., Cao, X., Wu, X.J., He, Q., Yang, J., Zhang, X., Chen, J., Zhao, W., Han, S., Nam, G.H., *et al.* (2017). Recent advances in ultrathin two-dimensional nanomaterials. Chem. Rev. *117*, 6225-6331.

10. Sun, Z.P., Martinez, A., and Wang, F. (2016). Optical modulators with 2D layered materials. Nat. Photon. *10*, 227-238.

11. Guo, W., Yu, C., Li, S.F., Song, X.D., Yang, Y., Qiu, B., Zhao, C.T., Huang, H.W., Yang, J., Han, X.T., *et al.* (2019). A phase transformation-resistant electrode enabled by a MnO_2-confined effect for enhanced energy storage. Adv. Funct. Mater. *29*, 1901342.

12. El-Kady, M.F., Ihns, M., Li, M.P., Hwang, J.Y., Mousavi, M.F., Chaney, L., Lech, A.T., and Kaner, R.B. (2015). Engineering three-dimensional hybrid supercapacitors and microsupercapacitors for high-performance integrated energy storage. Proc. Natl. Acad. Sci. USA *112*, 4233-4238.

13. Hu, Y.T., Wu, Y., and Wang, J. (2018). Manganese-oxide-based electrode materials for energy storage applications: how close are we to the theoretical capacitance? Adv. Mater. *30*, 1802569.

14. Guo, W., Yu, C., Li, S.F., Yang, J., Liu, Z.B., Zhao, C.T., Huang, H.W., Zhang, M.D., Han, X.T., Niu, Y.Y., *et al.* (2017). High-stacking-density, superior-roughness LDH bridged with vertically aligned graphene for high-performance asymmetric supercapacitors. Small *13*, 1701288.

15. Liu, J.Q., Zheng, M.B., Shi, X.Q., Zeng, H.B., and Xia, H. (2016). Amorphous FeOOH quantum dots assembled mesoporous film anchored on graphene nanosheets with superior electrochemical performance for supercapacitors. Adv. Funct. Mater. *26*, 919-930.

16. Li, Q., Xu, Y., Zheng, S., Guo, X., Xue, H., and Pang, H. (2018). Recent progress in some amorphous materials for supercapacitors. Small *14*, 1800426.

17. Shi, P.P., Li, L., Hua, L., Qian, Q.Q., Wang, P.F., Zhou, J.Y., Sun, G.Z., and Huang, W. (2017). Design of amorphous manganese oxide@multiwalled carbon nanotube fiber

for robust solid-state supercapacitor. ACS Nano *11*, 444-452.

18. Zhao, Y., Zheng, L., Shi, R., Zhang, S., Bian, X., Wu, F., Cao, X., Waterhouse, G.I.N., and Zhang, T. (2020). Alkali etching of layered double hydroxide nanosheets for enhanced photocatalytic N_2 reduction to NH_3. Adv. Energy Mater. *10*, 2002199.

19. Zhao, Y., Zhao, Y., Shi, R., Wang, B., Waterhouse, G.I.N., Wu, L.Z., Tung, C.H., and Zhang, T. (2019). Tuning oxygen vacancies in ultrathin TiO_2 nanosheets to boost photocatalytic nitrogen fixation up to 700 nm. Adv. Mater. *31*, 1806482.

20. Li, C., Wang, T., Zhao, Z.J., Yang, W., Li, J.F., Li, A., Yang, Z., Ozin, G.A., and Gong, J. (2018). Promoted fixation of molecular nitrogen with surface oxygen vacancies on plasmon-enhanced TiO_2 photoelectrodes. Angew. Chem. Int. Ed. *57*, 5278-5282.

21. Yan, D., Li, Y., Huo, J., Chen, R., Dai, L., and Wang, S. (2017). Defect chemistry of nonprecious-metal electrocatalysts for oxygen reactions. Adv. Mater. *29*, 1606459.

22. Bai, S., Zhang, N., Gao, C., and Xiong, Y. (2018). Defect engineering in photocatalytic materials. Nano Energy *53*, 296-336.

23. Shi, R., Zhao, Y., Waterhouse, G.I.N., Zhang, S., and Zhang, T. (2019). Defect engineering in photocatalytic nitrogen fixation. ACS Catal. *9*, 9739-9750.

24. Wang, L., Zhang, Y., Chen, L., Xu, H., and Xiong, Y. (2018). 2D polymers as emerging materials for photocatalytic overall water splitting. Adv. Mater. *30*, 1801955.

25. Chen, J., Han, Y., Kong, X., Deng, X., Park, H.J., Guo, Y., Jin, S., Qi, Z., Lee, Z., Qiao, Z., *et al.* (2016). The origin of improved electrical double-layer capacitance by inclusion of topological defects and dopants in graphene for supercapacitors. Angew. Chem. Int. Ed. *55*, 13822-13827.

26. Li, H.B., Yu, M.H., Wang, F.X., Liu, P., Liang, Y., Xiao, J., Wang, C.X., Tong, Y.X., and Yang, G.W. (2013). Amorphous nickel hydroxide nanospheres with ultrahigh capacitance and energy density as electrochemical pseudocapacitor materials. Nat. Commun. *4*, 1894.

27. Owusu, K.A., Qu, L.B., Li, J.T., Wang, Z.Y., Zhao, K.N., Yang, C., Hercule, K.M., Lin, C., Shi, C.W., Wei, Q.L., *et al.* (2017). Low-crystalline iron oxide hydroxide nanoparticle anode for high-performance supercapacitors. Nat. Commun. *8*, 14264.

28. Yang, J., Yu, C., Fan, X.M., Liang, S.X., Li, S.F., Huang, H.W., Ling, Z., Hao, C., and Qiu, J.S. (2016). Electroactive edge site-enriched nickel-cobalt sulfide into graphene frameworks for high-performance asymmetric supercapacitors. Energy Environ. Sci. *9*, 1299-1307.

29. Guo, W., Yu, C., Zhao, C.T., Wang, Z., Li, S.F., Yu, J.H., Tan, X.Y., Xie, Y.Y., Yang, L., Huang, H.L., *et al.* (2020). Boosting charge storage in 1D manganese oxide-carbon composite by phosphorus-assisted structural modification for supercapacitor applications. Energy Storage Mater. *31*, 172-180.

30. Yang, P.Y., Wu, Z.Y., Jiang, Y.C., Pan, Z.C., Tian, W.C., Jiang, L., and Hu, L.F. (2018). Fractal $(Ni_xCo_{1-x})_9Se_8$ nanodendrite arrays with highly exposed surface for wearable, all-solid-state supercapacitor. Adv. Energy Mater. *8*, 1801392.

31. Guo, W., Yu, C., Li, S.F., Song, X.D., Huang, H.W., Han, X.T., Wang, Z., Liu, Z.B., Yu, J.H., Tan, X.Y., *et al.* (2019). A universal converse voltage process for triggering transition metal hybrids in situ phase restruction toward ultrahigh-rate supercapacitors.

Adv. Mater. *31*, 1901241.

32. Yan, Z., Sun, H., Chen, X., Liu, H., Zhao, Y., Li, H., Xie, W., Cheng, F., and Chen, J. (2018). Anion insertion enhanced electrodeposition of robust metal hydroxide/oxide electrodes for oxygen evolution. Nat. Commun. *9*, 2373.

33. Lim, J., Maiti, U.N., Kim, N.Y., Narayan, R., Lee, W.J., Choi, D.S., Oh, Y., Lee, J.M., Lee, G.Y., Kang, S.H.*, et al.* (2016). Dopant-specific unzipping of carbon nanotubes for intact crystalline graphene nanostructures. Nat. Commun. *7*, 10364.

34. Huang, H.W., Yu, C., Huang, H.L., Zhao, C.T., Qiu, B., Yao, X.C., Li, S.F., Han, X.T., Guo, W., Dai, L.M.*, et al.* (2019). Activation of transition metal oxides by in-situ electro-regulated structure-reconstruction for ultra-efficient oxygen evolution. Nano Energy *58*, 778-785.

35. Niu, S., Jiang, W.J., Wei, Z., Tang, T., Ma, J., Hu, J.S., and Wan, L.J. (2019). Se-doping activates FeOOH for cost-effective and efficient electrochemical water oxidation. J. Am. Chem. Soc. *141*, 7005-7013.

36. Lin, B., Zhu, X., Fang, L., Liu, X., Li, S., Zhai, T., Xue, L., Guo, Q., Xu, J., and Xia, H. (2019). Birnessite nanosheet arrays with high K content as a high-capacity and ultrastable cathode for K-ion batteries. Adv. Mater. *31*, 1900060.

37. Dong, Z.H., Lin, F., Yao, Y.H., and Jiao, L.F. (2019). Crystalline $Ni(OH)_2$/amorphous $NiMoO_x$ mixed-catalyst with Pt-like performance for hydrogen production. Adv. Energy Mater. *9*, 1902703.

38. Julien, C. (2003). Raman spectra of birnessite manganese dioxides. Solid State Ionics *159*, 345-356.

39. Yang, W.L., and Devereaux, T.P. (2018). Anionic and cationic redox and interfaces in batteries: Advances from soft X-ray absorption spectroscopy to resonant inelastic scattering. J. Power Sources *389*, 188-197.

40. Kuppan, S., Shukla, A.K., Membreno, D., Nordlund, D., and Chen, G. (2017). Revealing anisotropic spinel formation on pristine Li- and Mn-rich layered oxide surface and its impact on cathode performance. Adv. Energy Mater. *7*, 1602010.

41. Henderson, C.M.B., Cressey, G., and Redfern, S.A.T. (1995). Geological applications of synchrotron radiation. Radiat. Phys. Chem. *45*, 459-481.

42. Oishi, M., Yamanaka, K., Watanabe, I., Shimoda, K., Matsunaga, T., Arai, H., Ukyo, Y., Uchimoto, Y., Ogumi, Z., and Ohta, T. (2016). Direct observation of reversible oxygen anion redox reaction in Li-rich manganese oxide, Li_2MnO_3, studied by soft X-ray absorption spectroscopy. J. Mater. Chem. A *4*, 9293-9302.

43. Dey, A., Krishnamurthy, S., Bowen, J., Nordlund, D., Meyyappan, M., and Gandhiraman, R.P. (2018). Plasma jet printing and in situ reduction of highly acidic graphene oxide. ACS Nano *12*, 5473-5481.

44. Bao, J., Zhang, X.D., Fan, B., Zhang, J.J., Zhou, M., Yang, W.L., Hu, X., Wang, H., Pan, B.C., and Xie, Y. (2015). Ultrathin spinel-structured nanosheets rich in oxygen deficiencies for enhanced electrocatalytic water oxidation. Angew. Chem. Int. Ed. *54*, 7399-7404.

45. Fang, G.Z., Zhu, C.Y., Chen, M.H., Zhou, J., Tang, B.Y., Cao, X.X., Zheng, X.S., Pan, A.Q., and Liang, S.Q. (2019). Suppressing manganese dissolution in potassium manganate with rich oxygen defects engaged high-energy-density and durable aqueous
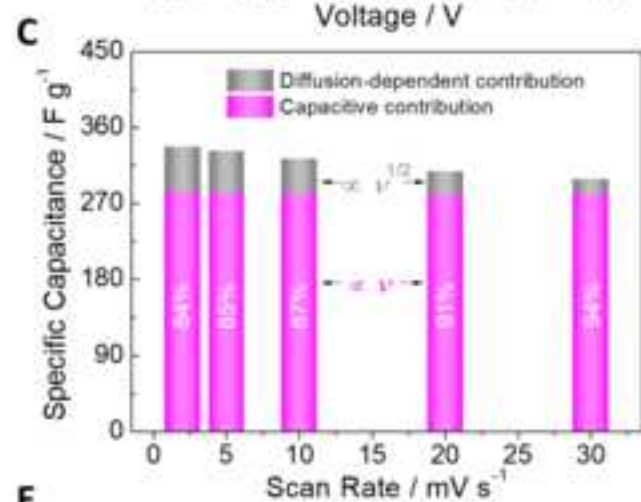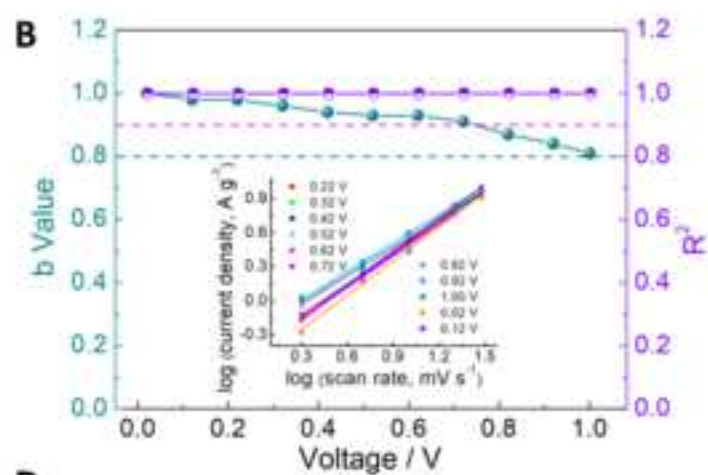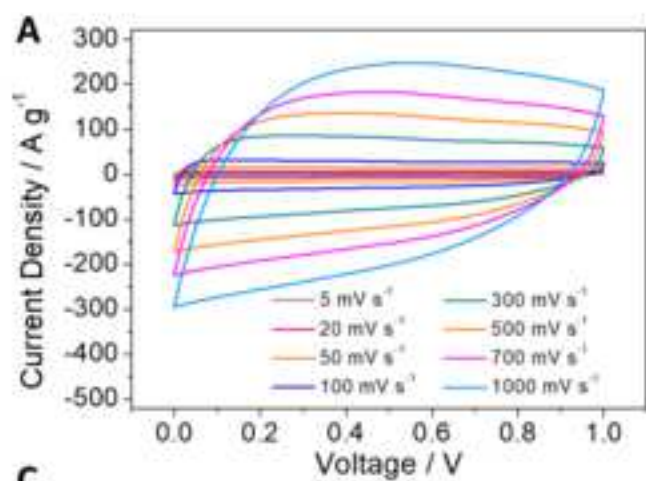
zinc-ion battery. Adv. Funct. Mater. *29*, 1808375.

46. Zhao, Y.X., Chang, C., Teng, F., Zhao, Y.F., Chen, G.B., Shi, R., Waterhouse, G.I.N., Huang, W.F., and Zhang, T.R. (2017). Defect-engineered ultrathin δ-MnO$_2$ nanosheet arrays as bifunctional electrodes for efficient overall water splitting. Adv. Energy Mater. *7*, 1700005.

47. Long, X., Yu, P., Zhang, N., Li, C., Feng, X., Ren, G., Zheng, S., Fu, J., Cheng, F., and Liu, X. (2019). Direct spectroscopy for probing the critical role of partial covalency in oxygen reduction reaction for cobalt-manganese spinel oxides. Nanomaterials *9*, 577.

48. Zhou, S.M., Miao, X.B., Zhao, X., Ma, C., Qiu, Y.H., Hu, Z.P., Zhao, J.Y., Shi, L., and Zeng, J. (2016). Engineering electrocatalytic activity in nanosized perovskite cobaltite through surface spin-state transition. Nat. Commun. *7*, 11510.

49. Zheng, X.L., Zhang, B., De Luna, P., Liang, Y.F., Comin, R., Voznyy, O., Han, L., García de Arquer, F.P., Liu, M., Dinh, C.T.*, et al.* (2018). Theory-driven design of high-valence metal sites for water oxidation confirmed using in situ soft X-ray absorption. Nat. Chem. *10*, 149-154.

50. Lin, F., Nordlund, D., Weng, T.-C., Zhu, Y., Ban, C., Richards, R.M., and Xin, H.L. (2014). Phase evolution for conversion reaction electrodes in lithium-ion batteries. Nat. Commun. *5*, 3358.

51. Zhu, X.H., Meng, F.Q., Zhang, Q.H., Xue, L., Zhu, H., Lan, S., Liu, Q., Zhao, J., Zhuang, Y.H., Guo, Q.B.*, et al.* (2020). LiMnO$_2$ cathode stabilized by interfacial orbital ordering for sustainable lithium-ion batteries. Nat. Sustain., https://doi.org/10.1038/s41893-41020-00660-41899.

52. Xia, Q., Zhang, Q., Sun, S., Hussain, F., Zhang, C., Zhu, X., Meng, F., Liu, K., Geng, H., Xu, J.*, et al.* (2020). Tunnel intergrowth Li$_x$MnO$_2$ nanosheet arrays as 3D cathode for high-performance all-solid-state thin film lithium microbatteries. Adv. Mater. *33*, 2003524.

53. Xu, W.J., Lyu, F.L., Bai, Y.C., Gao, A.Q., Feng, J., Cai, Z.X., and Yin, Y.D. (2018). Porous cobalt oxide nanoplates enriched with oxygen vacancies for oxygen evolution reaction. Nano Energy *43*, 110-116.

54. Wang, Y., Zhu, Y.L., Zhao, S.L., She, S.X., Zhang, F.F., Chen, Y., Williams, T., Gengenbach, T., Zu, L.H., Mao, H.Y.*, et al.* (2020). Anion etching for accessing rapid and deep self-reconstruction of precatalysts for water oxidation. Matter *3*, 2124-2137.

55. Clark, S.J., Segall, M.D., Pickard, C.J., Hasnip, P.J., Probert, M.I.J., Refson, K., and Payne, M.C. (2005). First principles methods using CASTEP. Z. Kristallogr. Cryst. Mater. *220*, 567-570.

56. Vanderbilt, D. (1990). Soft self-consistent pseudopotentials in a generalized eigenvalue formalism. Phys. Rev. B *41*, 7892-7895.

57. Perdew, J.P., Burke, K., and Ernzerhof, M. (1996). Generalized gradient approximation made simple. Phys. Rev. Lett. *77*, 3865-3868.

58. Dudarev, S.L., Botton, G.A., Savrasov, S.Y., Humphreys, C.J., and Sutton, A.P. (1998). Electron-energy-loss spectra and the structural stability of nickel oxide: An LSDA+U study. Phys. Rev. B *57*, 1505-1509.

59. Monkhorst, H.J., and Pack, J.D. (1976). Special points for Brillouin-zone integrations. Phys. Rev. B *13*, 5188-5192.

60. Zhao, Y.X., Chang, C., Teng, F., Zhao, Y.F., Chen, G.B., Shi, R., Waterhouse, G.I.N., Huang, W.F., and Zhang, T.R. (2017). Defect-engineered ultrathin δ-MnO_2 nanosheet arrays as bifunctional electrodes for efficient overall water splitting. Adv. Energy Mater. *7*, 1700005.

61. Yang, W., and Devereaux, T.P. (2018). Anionic and cationic redox and interfaces in batteries: Advances from soft X-ray absorption spectroscopy to resonant inelastic scattering. J. Power Sources *389*, 188-197.

62. Lin, F., Nordlund, D., Markus, I.M., Weng, T.-C., Xin, H.L., and Doeff, M.M. (2014). Profiling the nanoscale gradient in stoichiometric layered cathode particles for lithium-ion batteries. Energy Environ. Sci. *7*, 3077-3085.

Figure 1   Click here to access/download;Figure;Figure 1.tif ±

Figure 2   Click here to access/download;Figure;Figure 2.tif

Figure 3

Click here to access/download;Figure;Figure 3.tif ⬇

Figure 4

Click here to access/download;Figure;Figure 4.tif ±
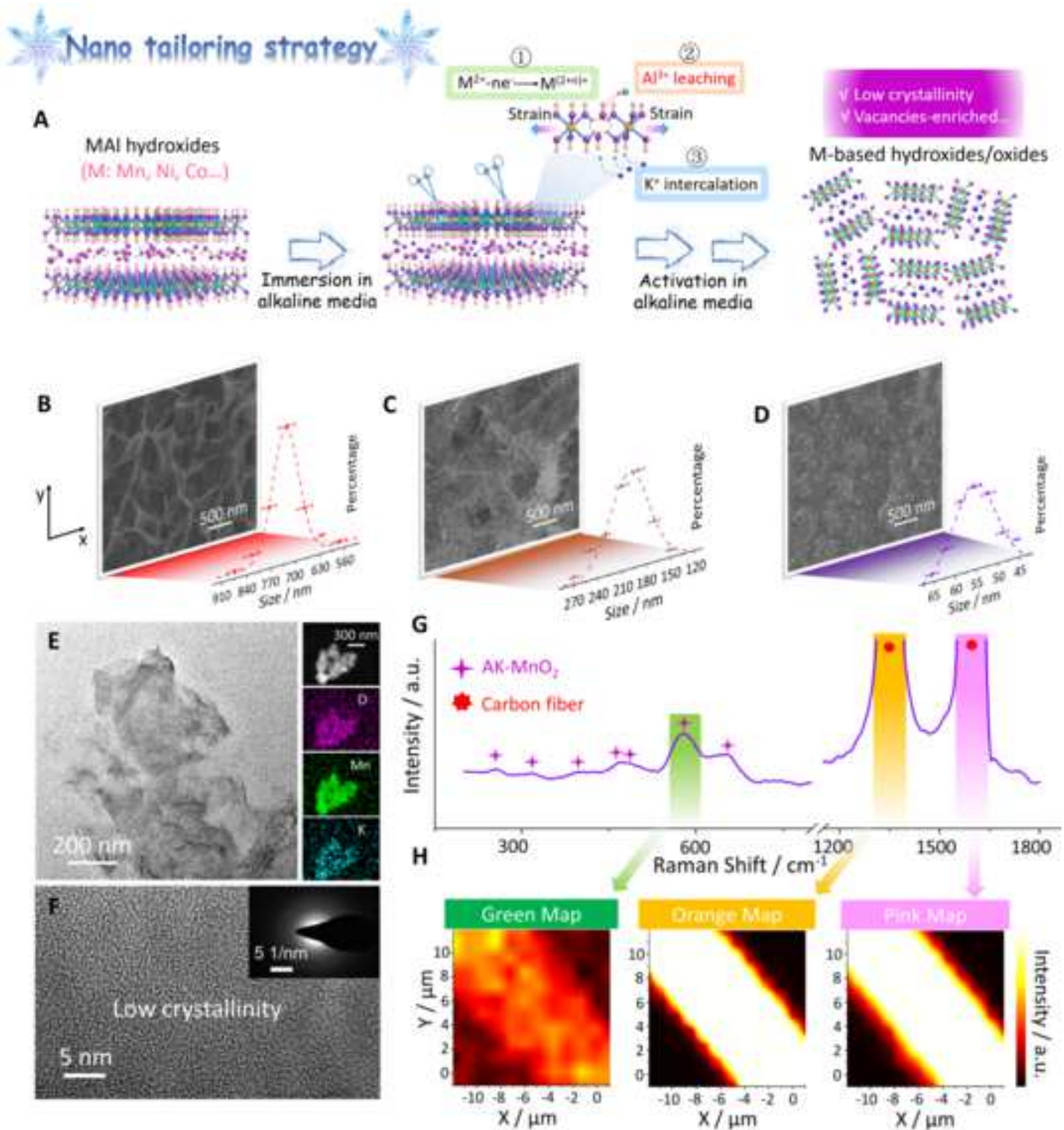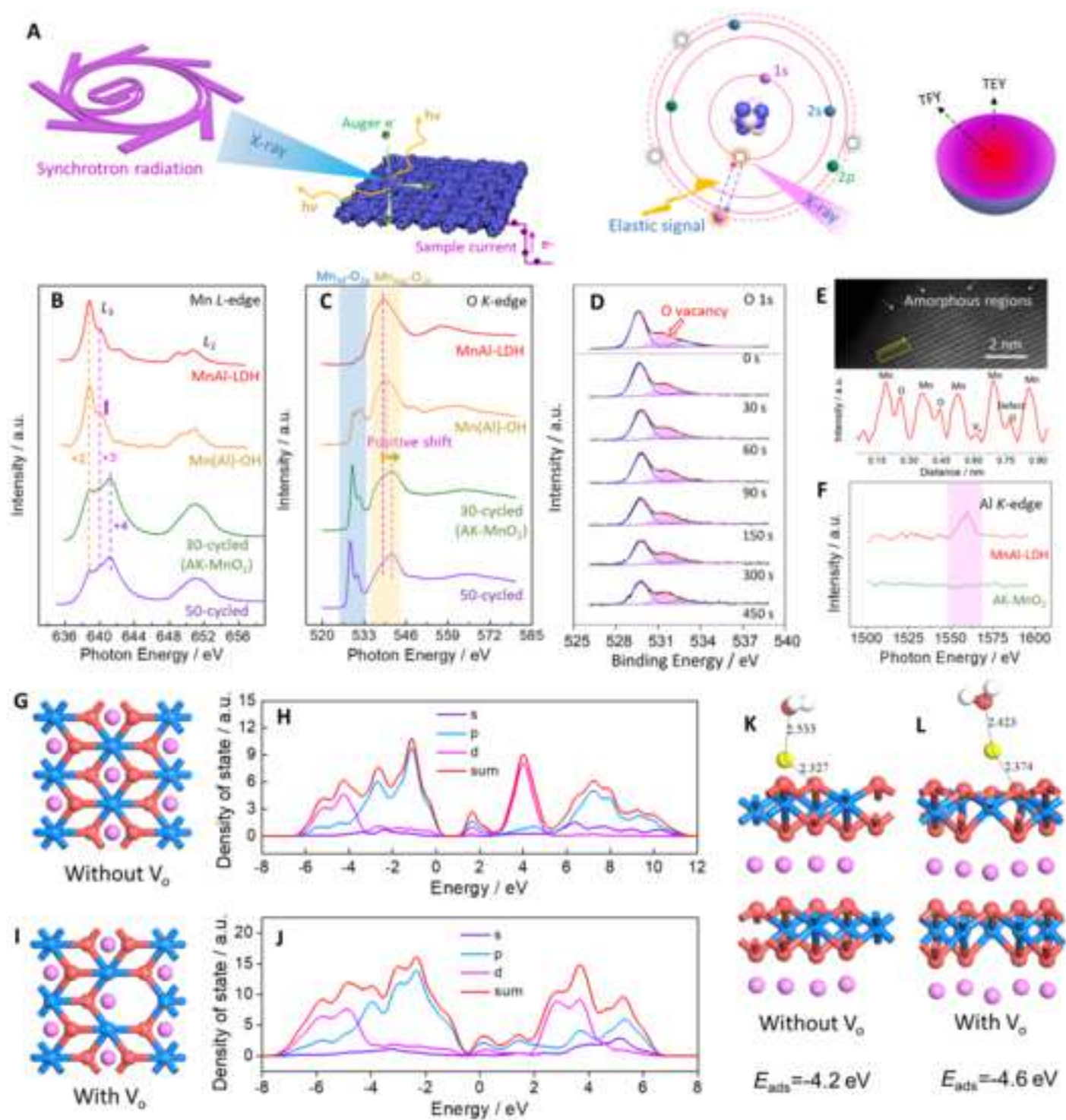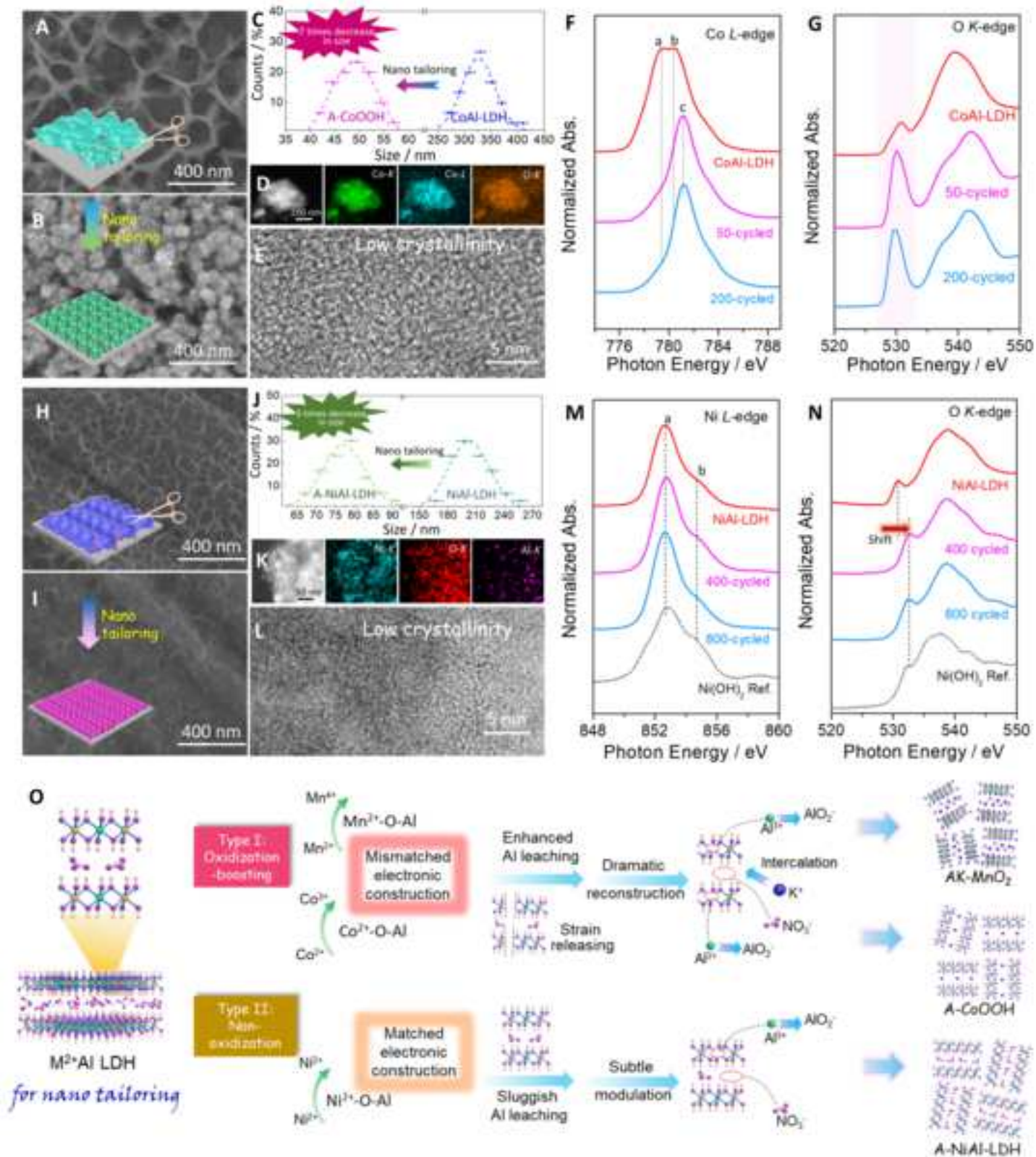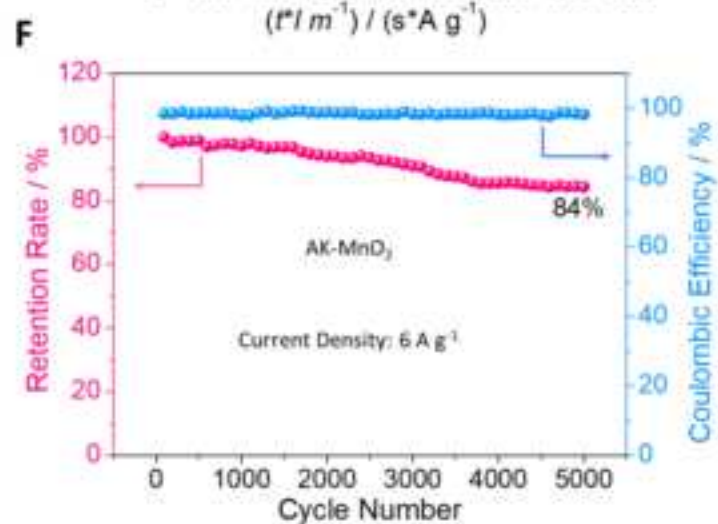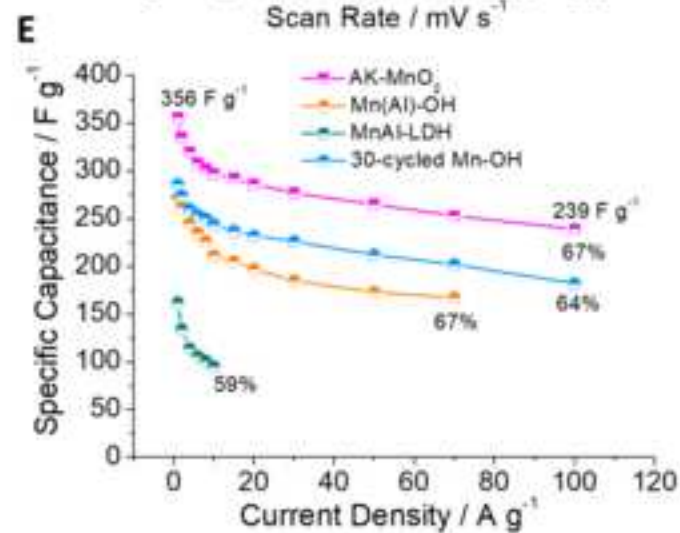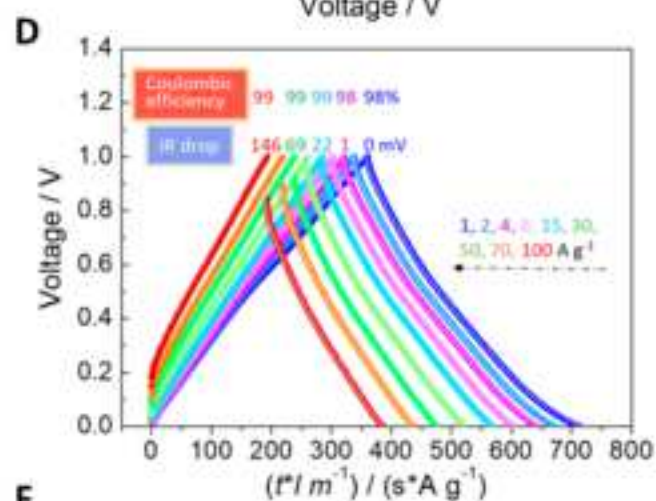
Supplemental Information for

Operando leaching of pre-incorporated Al and mechanism in transition metal hybrids on carbon substrates for elaborately enhanced charge storage

Wei Guo, Feipeng Yang, Chang Yu*, Yuanyang Xie, Jiuke Chen, Yisheng Liu, Yang Zhao, Juan Yang, Xuefei Feng, Shaofeng Li, Zhao Wang, Jinhe Yu, Kunlun Liu, Kun Qian, Mesfin Tsige, Qiuyu Zhang*, Jinghua Guo*, and Jieshan Qiu*

Supplemental Experimental Procedures

Fabrication of the CoAl-LDH, Co(Al)-OH and A-CoOOH

The CoAl-LDH was formed by the same procedure like MnAl-LDH except for the electrolyte. The adopted electrolyte was prepared by mixing 0.6 mmol $Co(NO_3)_2$ and 0.4 mmol $Al(NO_3)_3$ with 50 mL of deionized water. The formed CoAl-LDH hybrids were soaked in 6 M KOH electrolyte for 2 min. Then it was further cycled by a cyclic voltammetry technique with a voltage range of 0-0.6 V for 200 cycles, yielding A-CoOOH hybrids. In comparison, the CoAl-LDH hybrids were also treated by 50 cycles. And the Co(Al)-OH hybrids were formed following the same process without cyclic voltammetry treatment. Further, $Co(OH)_2$ was formed following our previous work.[1] The as formed hybrids were washed by water and ethanol for several times, and then dried at 60 °C for 2 h.

Fabrication of the NiAl-LDH and A-NiAl-LDH

The NiAl-LDH was also formed following the same procedure as MnAl-LDH. The adopted electrolyte was prepared by mixing 0.6 mmol $Ni(NO_3)_2$ and 0.4 mmol $Al(NO_3)_3$ with 50 mL of deionized water. The formed NiAl-LDH hybrids were soaked for 2 min in 6 M KOH electrolyte. Then it was cycled by a cyclic voltammetry technique with a voltage range of 0-0.6 V for 400 cycles, yielding A-NiAl-LDH hybrids. In comparison, the NiAl-LDH hybrids were also treated by 30, 90, 200 and 800 cycles.

Material characterization

The as-made composite materials were characterized by cold field emission SEM (HITACHI UHR FE-SEM SU8220), TEM, HR-TEM and HAADF-STEM (FEI Tecnai G2 F30, FEI Themis Z), XRD (Cu Kα, λ=1.5406 Å), AFM (Dimension Icon), XPS (Thermo ESCALAB 250), and Raman spectroscopy (HORIBA LabRAM HR Evolution Raman Microscope). Mn *L*-edge and O, Al, C *K*-edge soft XAS measurements were conducted at Beamline 7.3.1 of Advanced Light Source, Lawrence Berkeley National Laboratory, as well as Beamline BL14W1 station in Shanghai Synchrotron Radiation Facility (SSRF).

Electrochemical characterization

The electrochemical performance of the as-made electrodes was evaluated in a three-electrode cell. For Mn-based hybrids, the Ag/AgCl and Pt sheet were used as reference and counter electrodes. The adopted electrolyte is 1 M aqueous Na_2SO_4 solution. For Ni- or Co- based hybrids, the Hg/HgO and Pt sheet were used as the reference and counter electrodes, and the adopted electrolyte is 6 M aqueous KOH solution. The capacitance value of the electrode was determined by the following equation:

$C=(I\Delta t) / (m\Delta V)$

where C is the specific capacitance (F g^{-1}), ΔV is the voltage range after ohmic drop (V), I is the discharge current (A), Δt is the discharge time (s), m is the weight of active materials on the CP (g).
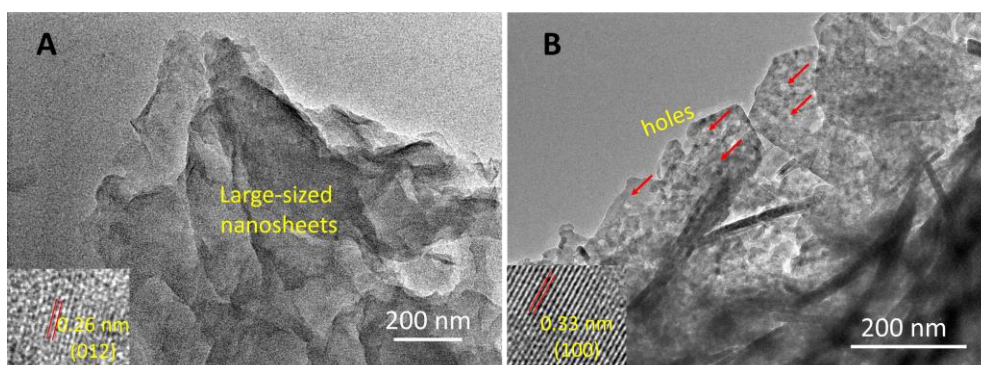
Figure S1. A, B, TEM and HR-TEM images: (A) MnAl-LDH and (B) Mn(Al)-OH nanosheets.
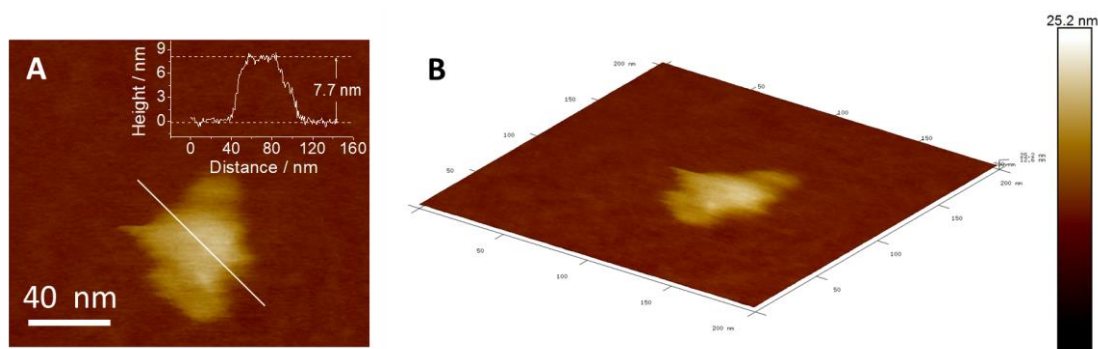
Figure S2. A, B, AFM images of the AK-MnO$_2$ nanosheet.
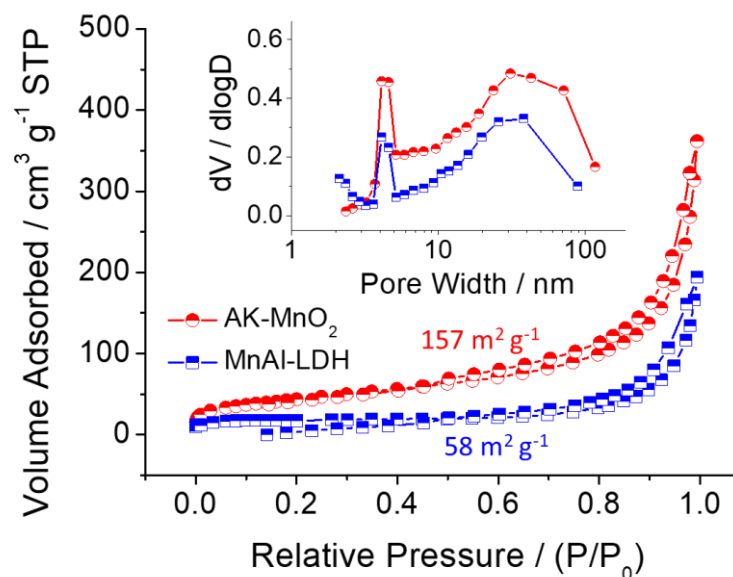
Figure S3. Nitrogen adsorption-desorption isotherms, and the corresponding pore size distributions of the MnAl-LDH and AK-MnO$_2$.
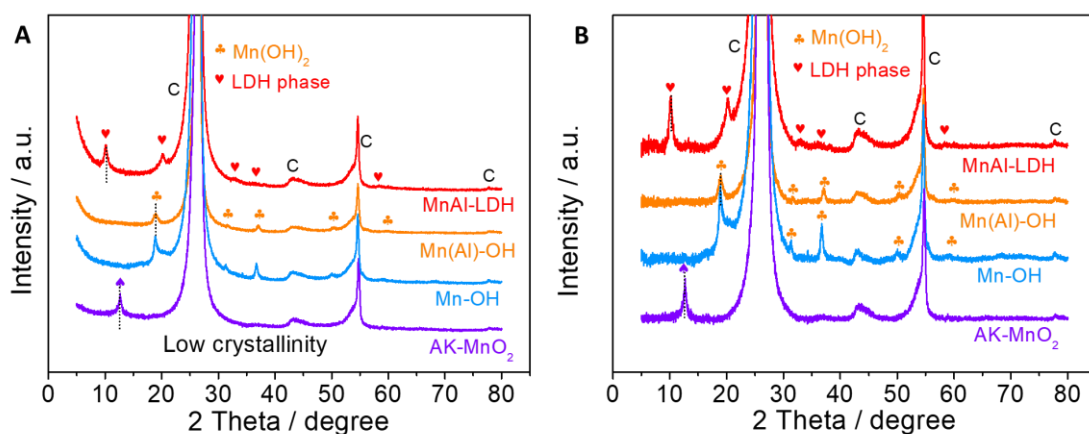
Figure S4. A, B, XRD patterns (A) of the MnAl-LDH, Mn(Al)-OH, Mn-OH and AK-MnO$_2$ and that (B) after being magnified and subtracting the baselines.
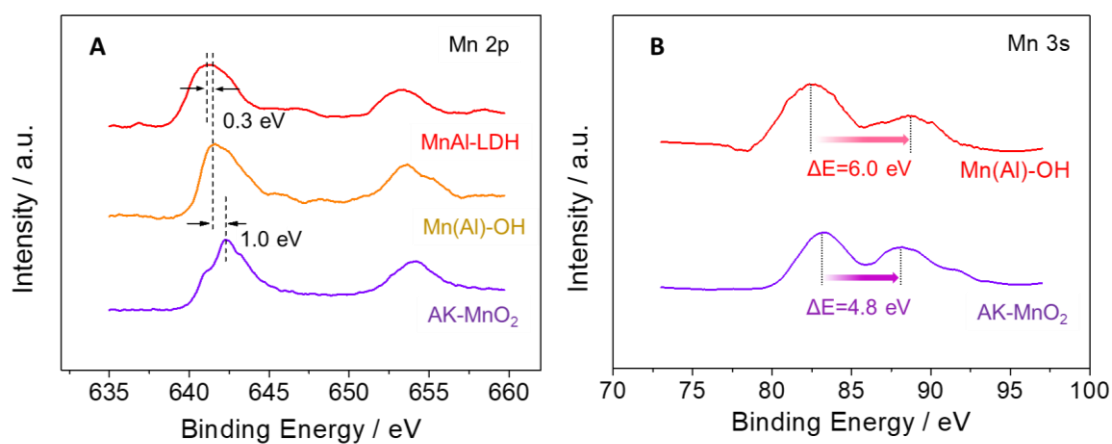
Figure S5. A, Mn 2p XPS spectra for the MnAl-LDH, Mn(Al)-OH and AK-MnO$_2$ hybrids, where the positive shift of Mn 2p spectra corresponds to the oxidation of Mn ions. B, Mn 3s XPS spectra for the Mn(Al)-OH and AK-MnO$_2$ hybrids, where the peak separation of Mn 3s it displays a significant decrease from 6.0 V to 4.8 V, further confirming the significant oxidation after the electrochemical cycle process.[2]
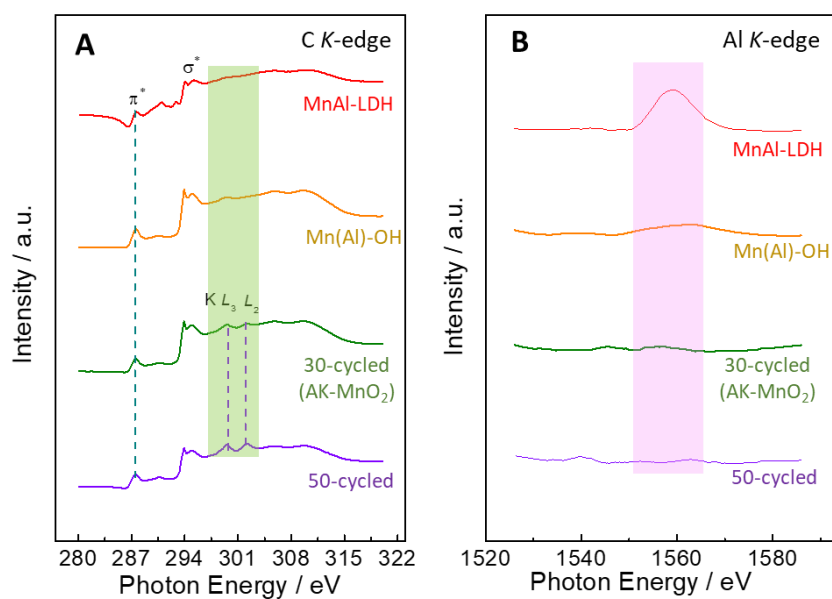
Figure S6. A, B, sXAS spectra (TEY mode) of the MnAl-LDH, Mn(Al)-OH and the 30-cycled (AK-MnO$_2$) and 50-cycled hybrids: (A) C *K*-edge and (B) Al *K*-edge.
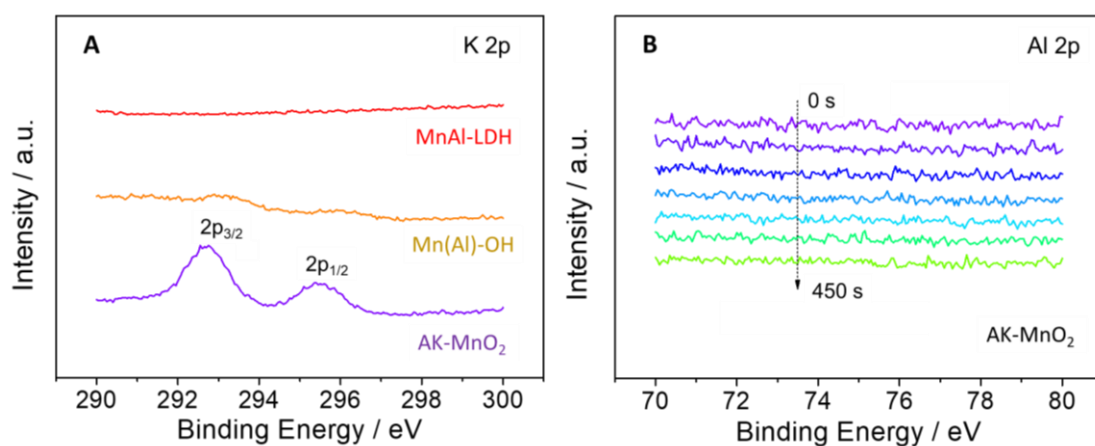
Figure S7. A, K 2p XPS spectra for MnAl-LDH, Mn(Al)-OH and AK-MnO$_2$ hybrids. B, Depth XPS spectra for AK-MnO$_2$ hybrids.
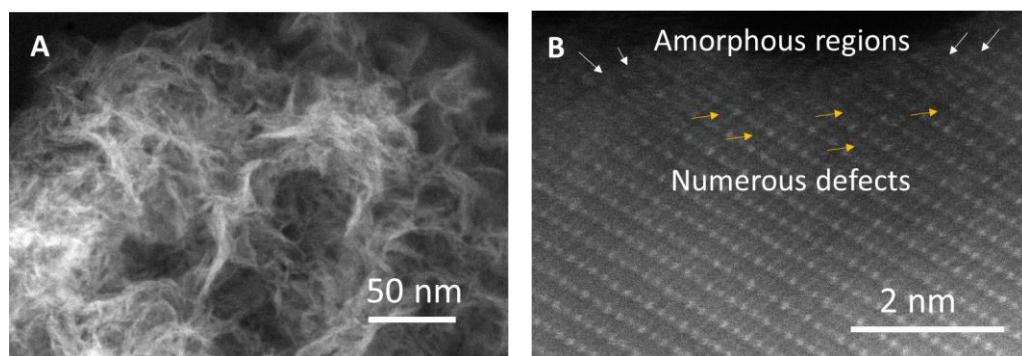
Figure S8. A, B, HAADF-STEM images of the AK-MnO$_2$.
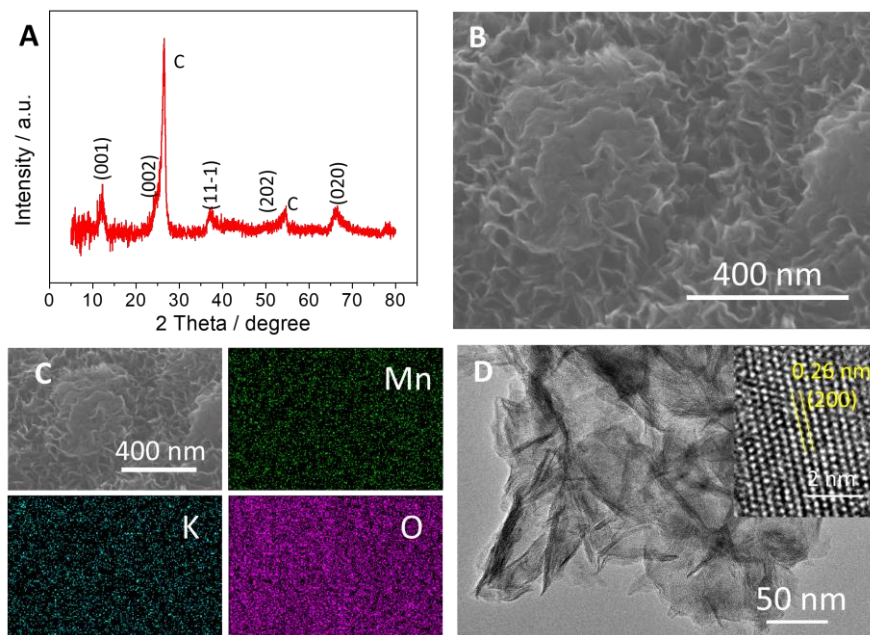
Figure S9. A, XRD pattern of the HC-MnO$_2$, where the diffraction peaks can be well matched with the standard PDF card of birnessite-type MnO$_2$ (JCPDS card no. 43-1456); B, C, SEM image (B) and the corresponding elemental mapping images (C) of the HC-MnO$_2$; D, TEM image of the HC-MnO$_2$. The inset is the corresponding HR-TEM image, where the interplanar spacing is identified to be 0.26 nm, in good accordance with (200) plane of birnessite-type MnO$_2$.
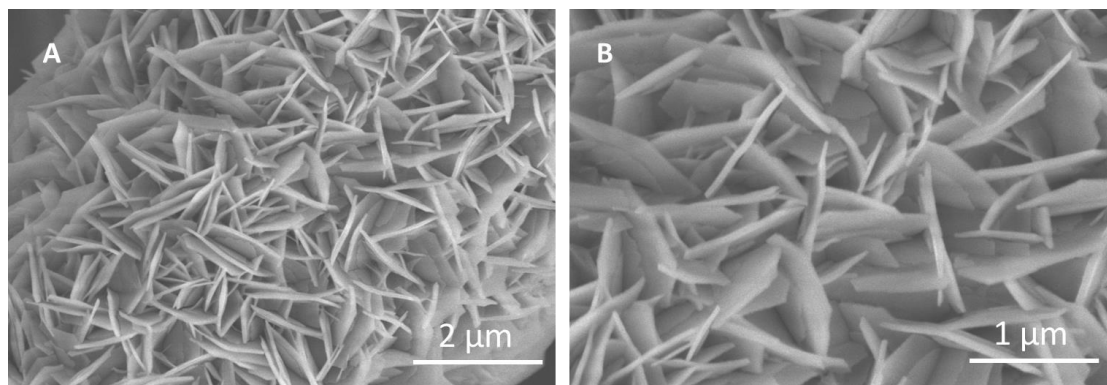
Figure S10. A, B, SEM images of the Mn-OH without the addition of Al source.
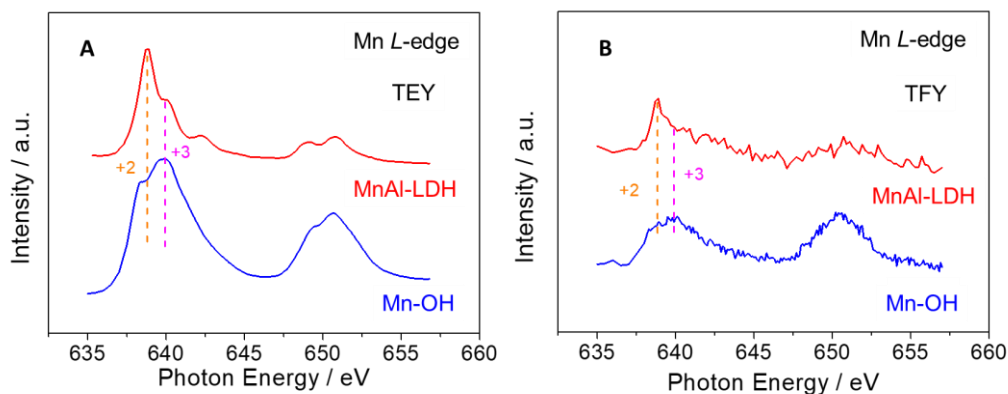
Figure S11. A, B, Comparison of Mn *L*-edge soft XAS spectra for the MnAl-LDH and Mn-OH: (A) TEY scans and (B) TFY scans. A higher Mn valence is displayed for the Mn-OH than that of the MnAl-LDH, implying that the formation of LDH phase can help resist the oxidation of Mn sites.
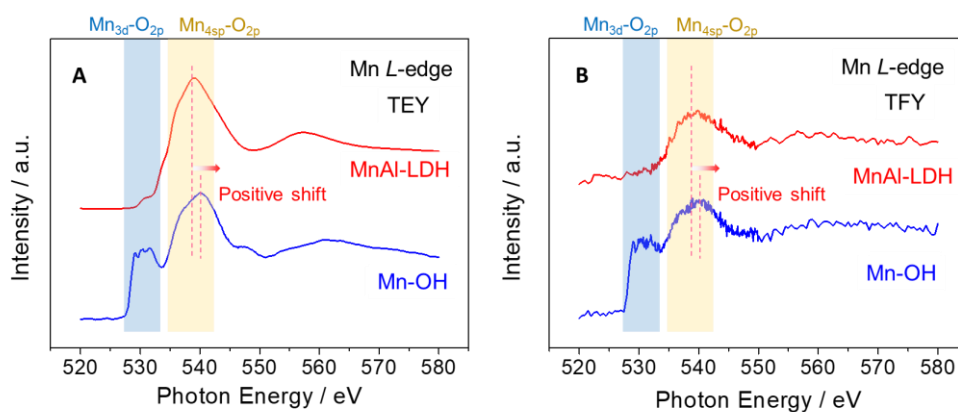
Figure S12. A, B, Soft XAS spectra comparison of O *K*-edge for the MnAl-LDH and Mn-OH: (A) TEY scans and (B) TFY scans.
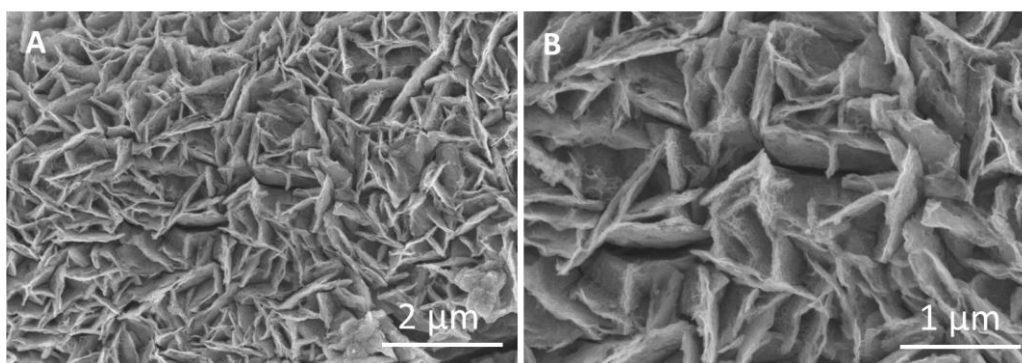
Figure S13. A, B, SEM images of the Mn-OH after 30 electrochemical cycles in 6 M KOH electrolyte, demonstrating the formation of large-sized heterostructure rather than the small-sized microstructure like the AK-MnO$_2$.
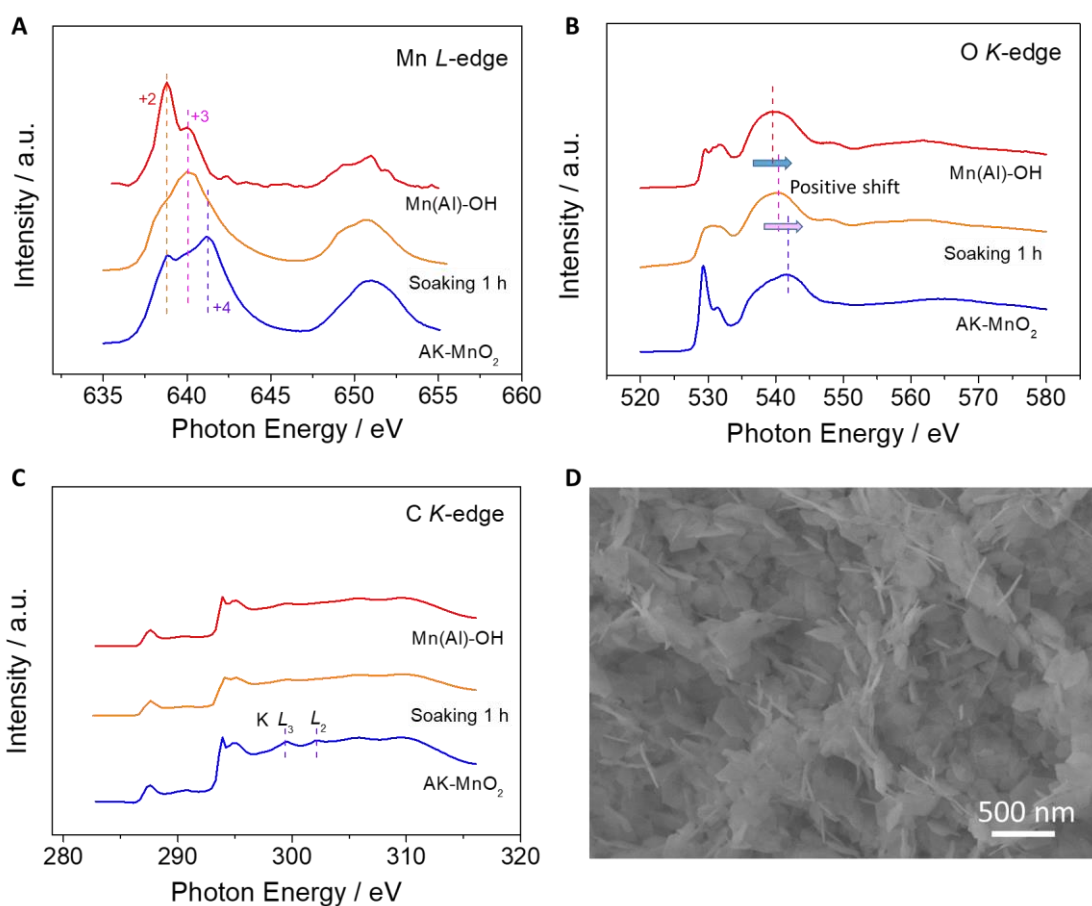
Figure S14. A-C, Mn *L*-edge (A), O *K*-edge (B) and C *K*-edge (C) spectra of the MnAl-LDH after soaking in 6 M KOH for 1 h and the comparison with those of the Mn(Al)-OH and AK-MnO$_2$, demonstrating the incomplete oxidation and phase transformation. D, SEM image of the MnAl-LDH after being soaked in 6 M KOH for 1 h, where the size is much larger than that of the AK-MnO$_2$.
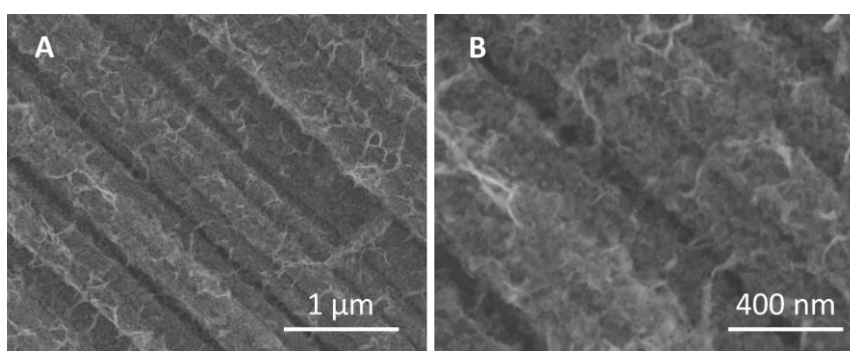
Figure S15. A, B, SEM images of the CoAl-LDH after soaking in 6 M KOH for 2 min (Co(Al)-OH), demonstrating that the nanosheets are partially broken due to fast Al leaching process.
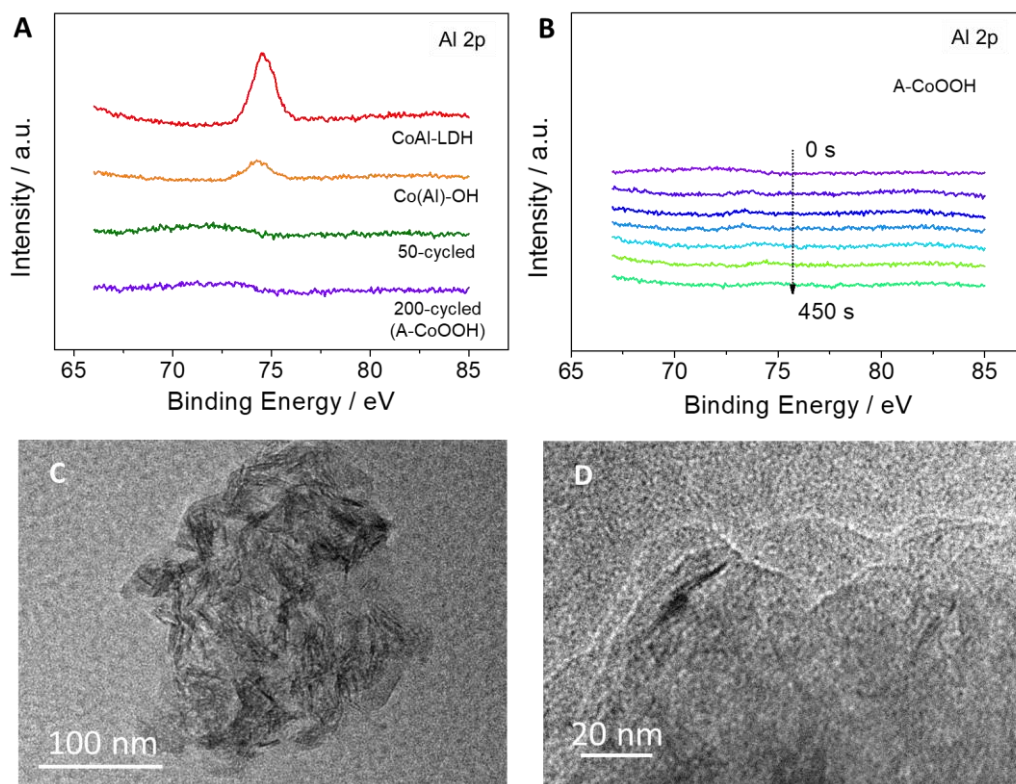
Figure S16. A, *Ex-situ* Al 2p XPS spectra of the pristine CoAl-LDH, the Co(Al)-OH and the formed 50-cycled and 200-cycled (A-CoOOH) hybrids, demonstrating the gradual decrease of Al 2p signal. B, Depth Al 2p XPS spectra of the A-CoOOH hybrids. C, D, TEM images of the A-CoOOH hybrids.
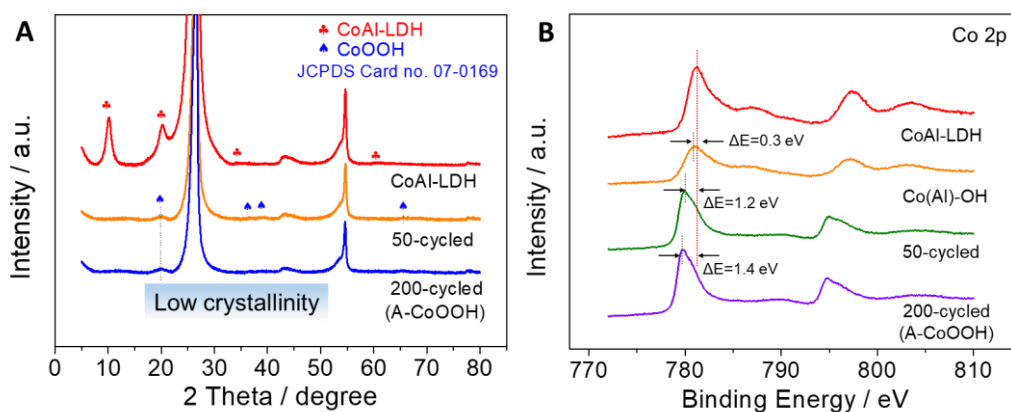
Figure S17. A, XRD patterns of the pristine CoAl-LDH and that after 50 and 200 cycles (A-CoOOH). B, Co 2p XPS spectra of the CoAl-LDH, the Co(Al)-OH, and the formed 50-cycled and 200-cycled (A-CoOOH) hybrids, where the negative shift of Co 2p spectrum attributes to the oxidation of Co sites.[1]
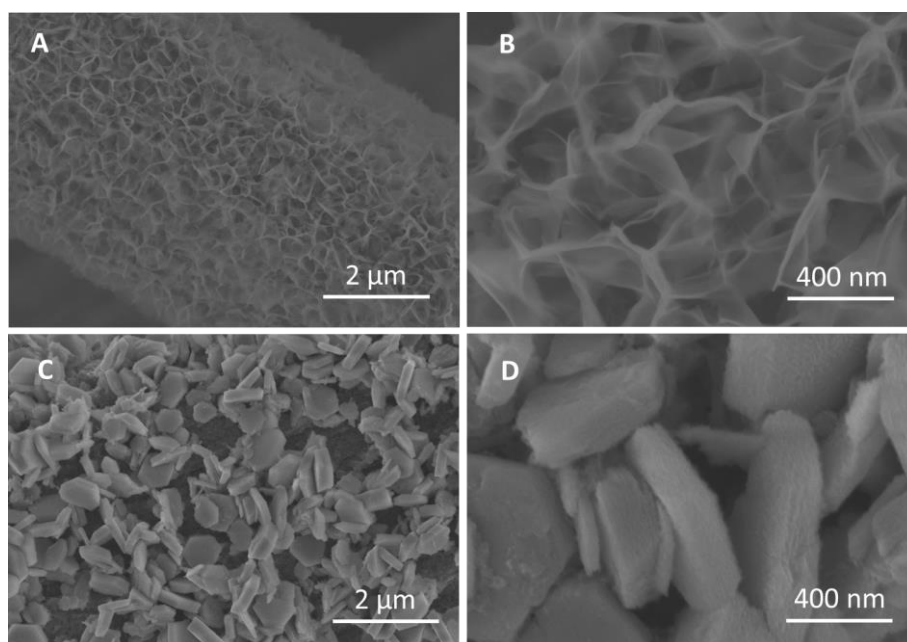
Figure S18. A-D, SEM images of (A-B) the pristine $Co(OH)_2$ and (C-D) that after 50 cycles in 6 M KOH electrolyte.
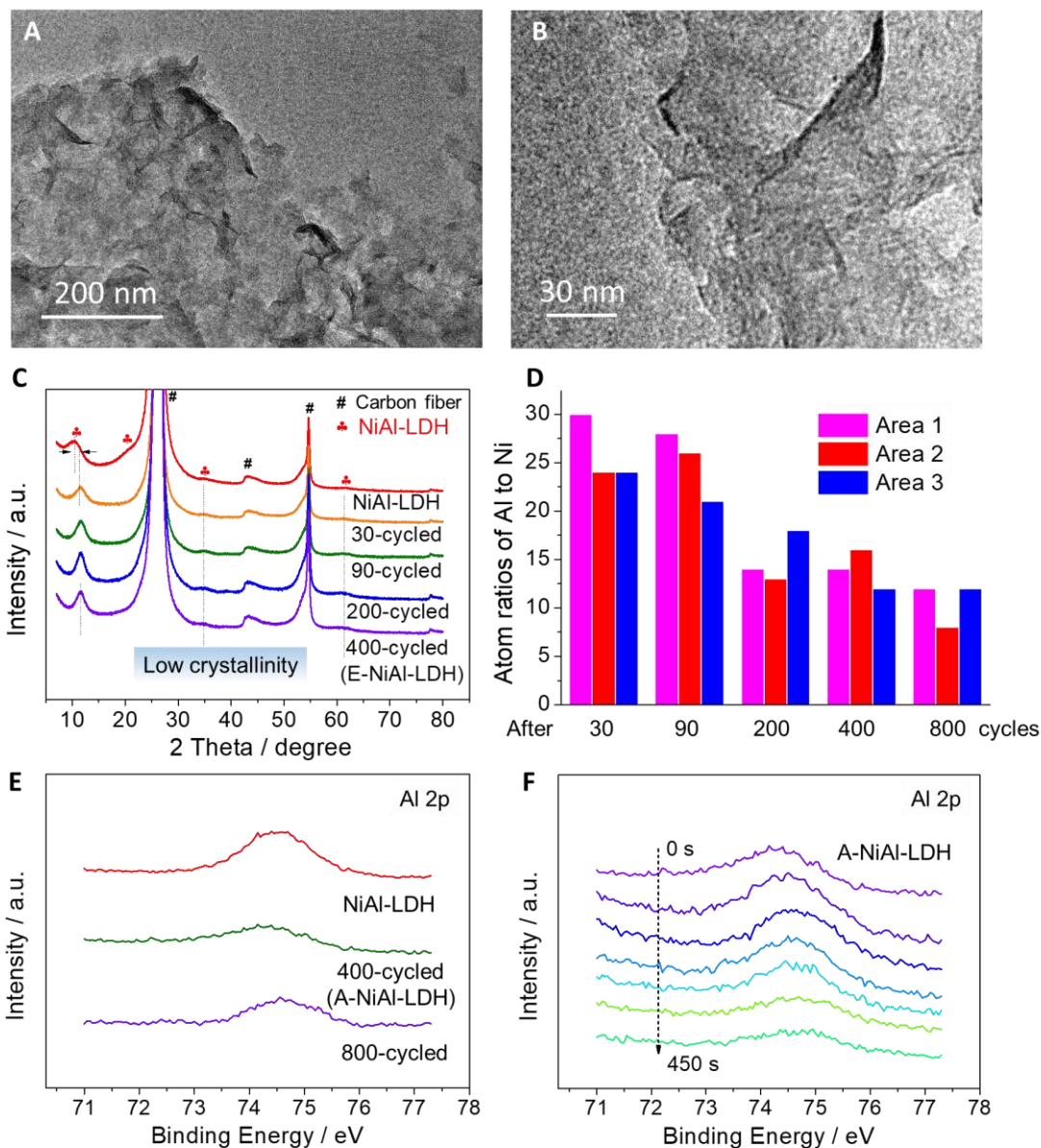
Figure S19. A, B, TEM images of the A-NiAl-LDH hybrids. C, XRD patterns for the NiAl-LDH before and after different cycles in alkaline electrolyte, where the low-crystallinity/amorphous features of the [(Ni/Al)O$_6$] laminate are observed after 400 cycles. The shrinkage of the interlayer spacing attributes to the releasing of interlayer anions, accompanied by the leaching of Al to keep the charge balance. D, Atom ratios of Al to Ni after different CV cycles in three different regions, according to SEM/EDS results. The ratio decreases to about 10%-15% after 400 cycles and no more obvious decrease is found after 800 cycles. E, Al 2p XPS spectra of the pristine NiAl-LDH and that after 400 (A-NiAl-LDH) and 800 cycles. F, Depth Al 2p XPS spectra of the A-NiAl-LDH hybrids.
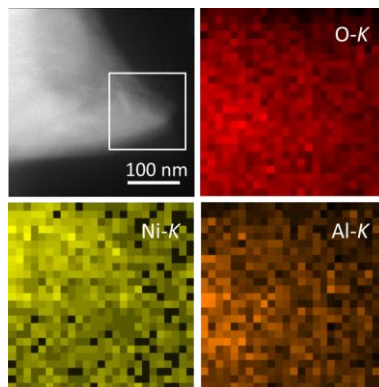
12

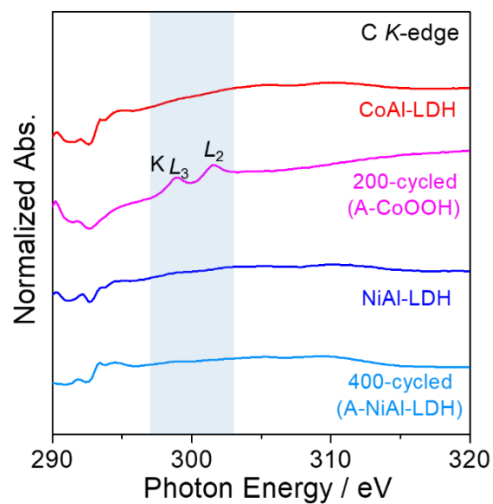**Figure S20.** HAADF-STEM image of the pristine NiAl-LDH hybrids and the corresponding EDS mapping images.

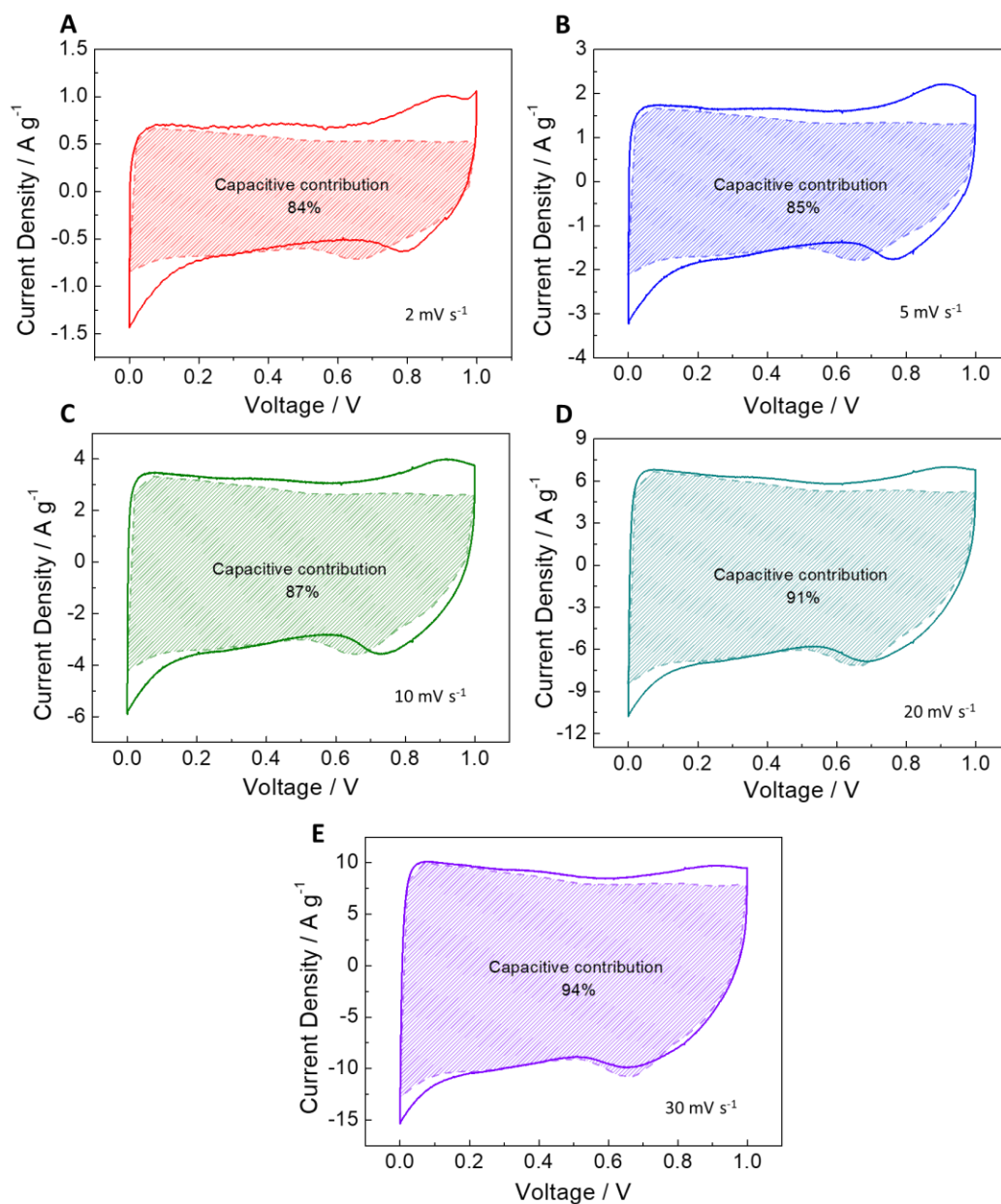**Figure S21.** C *K*-edge spectra of the CoAl-LDH, A-CoOOH, NiAl-LDH and A-NiAl-LDH.

Figure S22. A-E, Capacitive contribution of the AK-MnO$_2$ hybrids at different scan rates, according to Dunn's method:[3-4] (A) 2 mV s^{-1}, (B) 5 mV s^{-1}, (C) 10 mV s^{-1}, (D) 20 mV s^{-1} and (E) 30 mV s^{-1}.
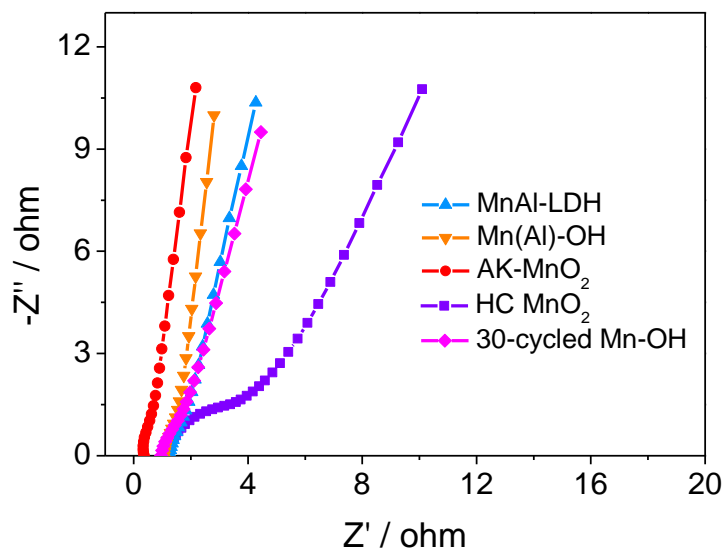
Figure S23. Nyquist plots of the MnAl-LDH, Mn(Al)-OH, AK-MnO$_2$, HC-MnO$_2$ and 30-cycled Mn-OH.
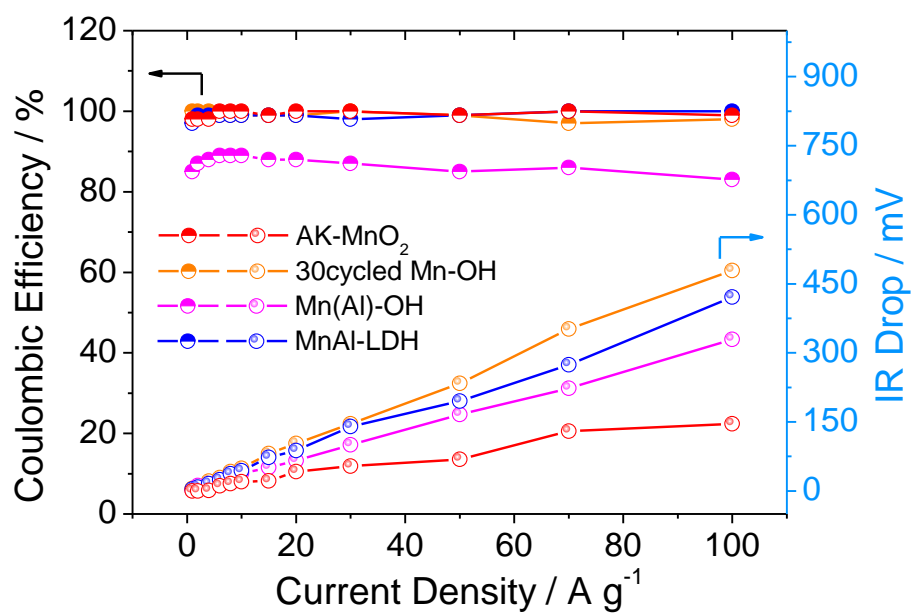

Figure S24. A comparison for the Coulombic efficiencies and IR drops of the AK-MnO$_2$ and the counterparts.
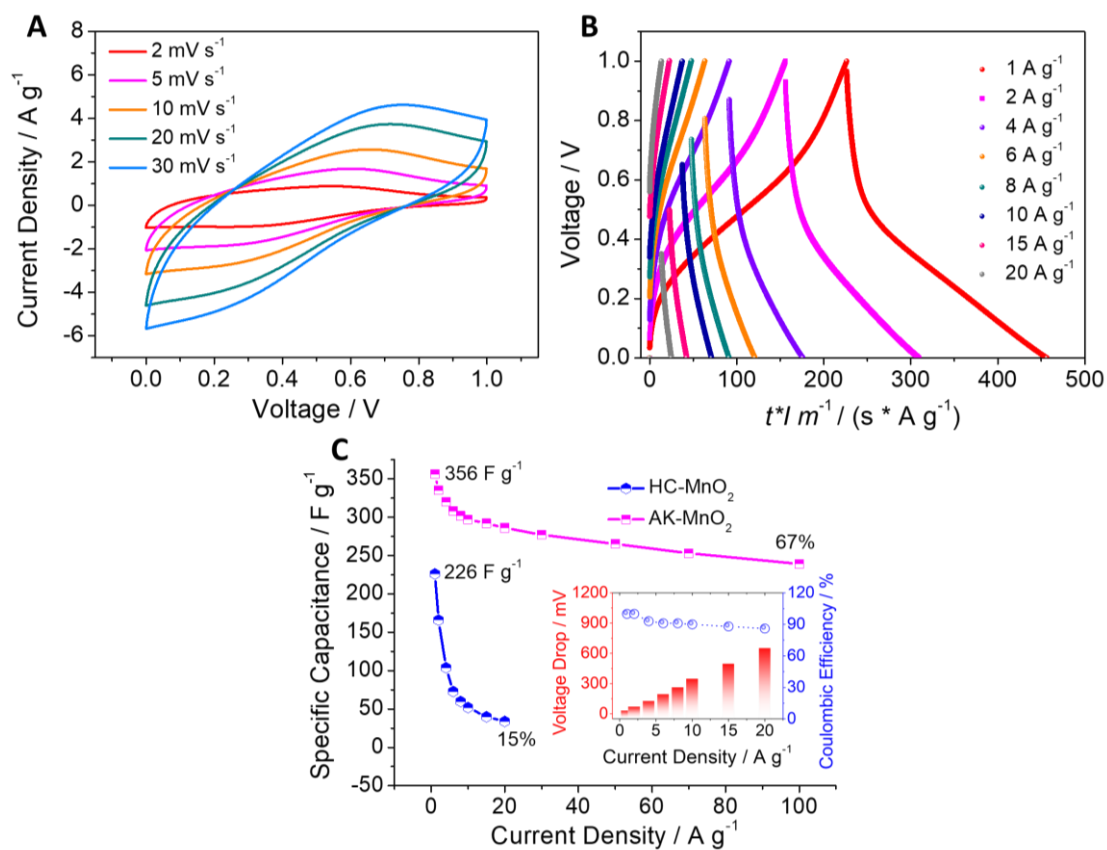
Figure S25. A-C Electrochemical performance of the HC-MnO$_2$: (A) CV curves and (B) GCD curves of the HC-MnO$_2$. (C) A comparison for the specific capacitance of the HC-MnO$_2$ and AK-MnO$_2$ at different current densities, where the inset is the voltage drop and Coulombic efficiency of the HC-MnO$_2$ at different current densities.
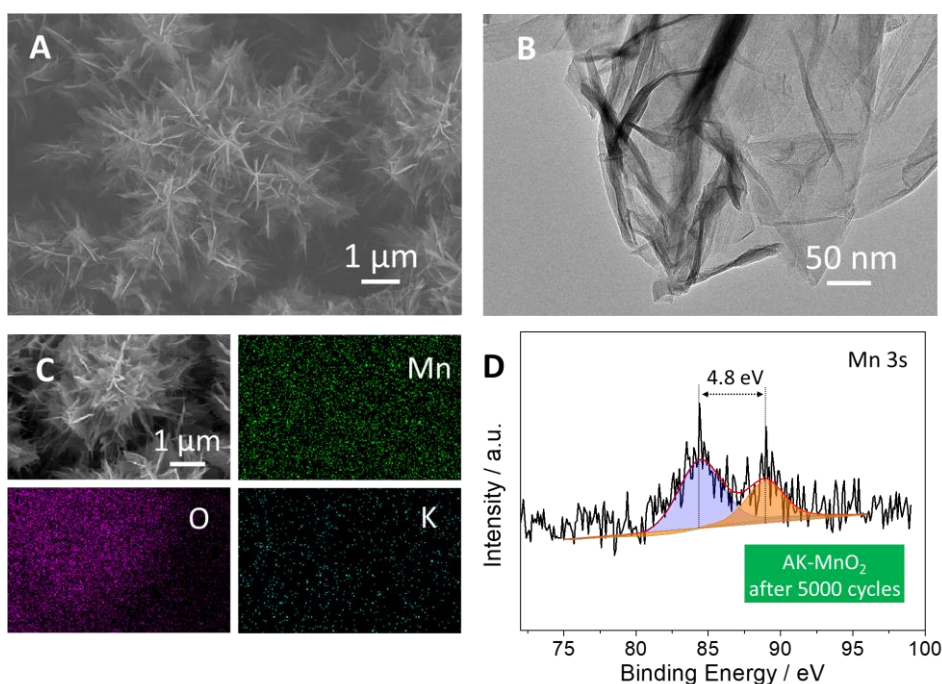
Figure S26. A, B, SEM (A) and TEM (B) images of the AK-MnO$_2$, demonstrating the well-kept nanosheet morphology. C, SEM elemental mapping images of the AK-MnO$_2$ after 5000 cycles, demonstrating the homogeneous distribution of Mn, O and K elements. D, Mn 3s XPS spectrum of the AK-MnO$_2$ after 5000 cycles. The spin-energy separation of 4.8 eV manifests the Mn^{4+}-dominated feature similar to its pristine status.
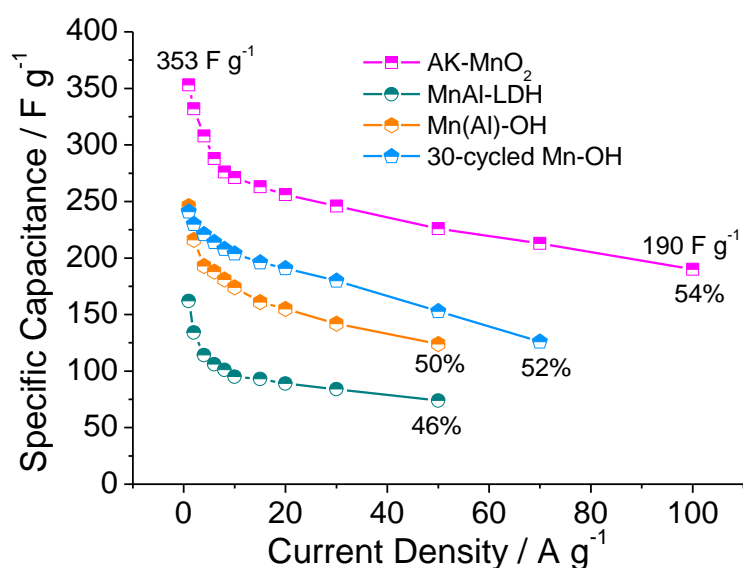

Figure S27. Specific capacitance of the MnAl-LDH, Mn(Al)-OH, 30-cycled Mn-OH, and AK-MnO$_2$ with the same mass loading (0.9±0.1 mg cm^{-2}) at different current densities.
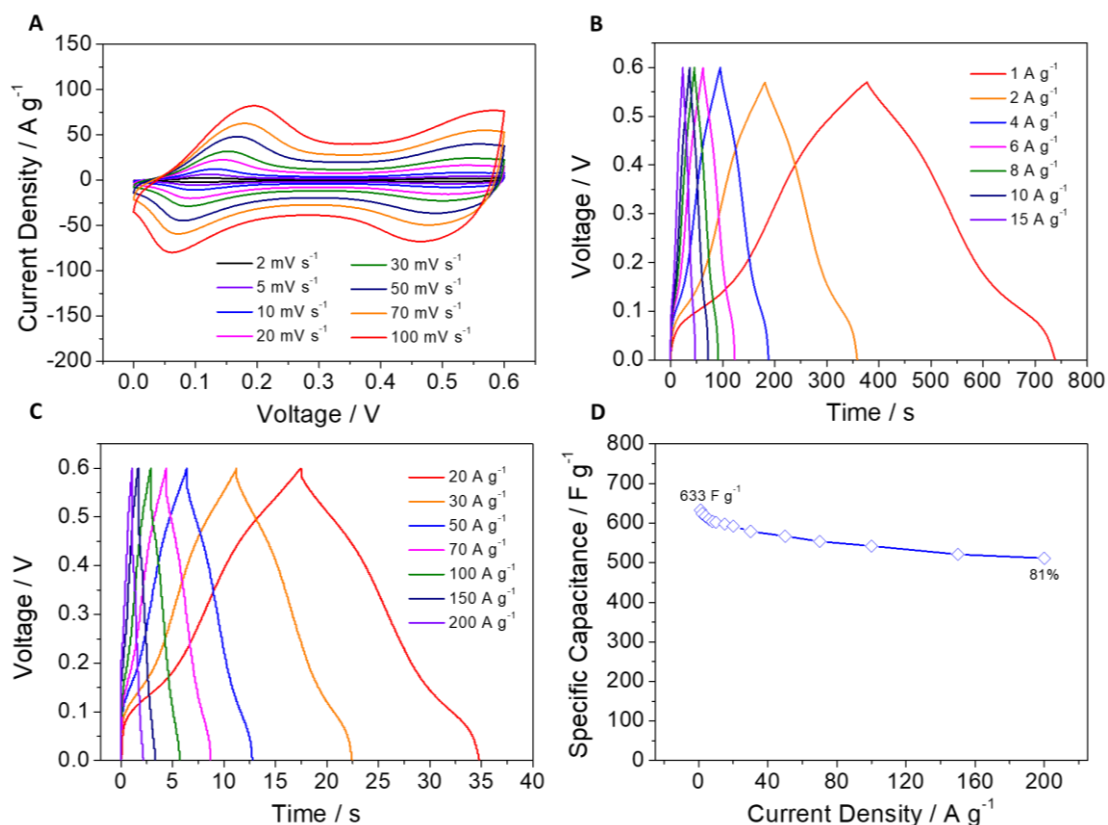
Figure S28. A, CV curves of the A-CoOOH hybrids from 2 mV s^{-1} to 100 mV s^{-1}. Two pairs of redox peaks at different scan rates can be found, corresponding to the Co^{2+}/Co^{3+} and Co^{3+}/Co^{4+} redox features, respectively. B, C, GCD curves of the A-CoOOH hybrids at different current densities changing (B) from 1 A g^{-1} to 15 A g^{-1} and (C) from 20 A g^{-1} to 200 A g^{-1}. D, Specific capacitance of the A-CoOOH hybrids at different current densities, which displays a superb capacitance value of 633 F g^{-1} at 1 A g^{-1} with a remarkable rate performance of 81% at 200 A g^{-1}.
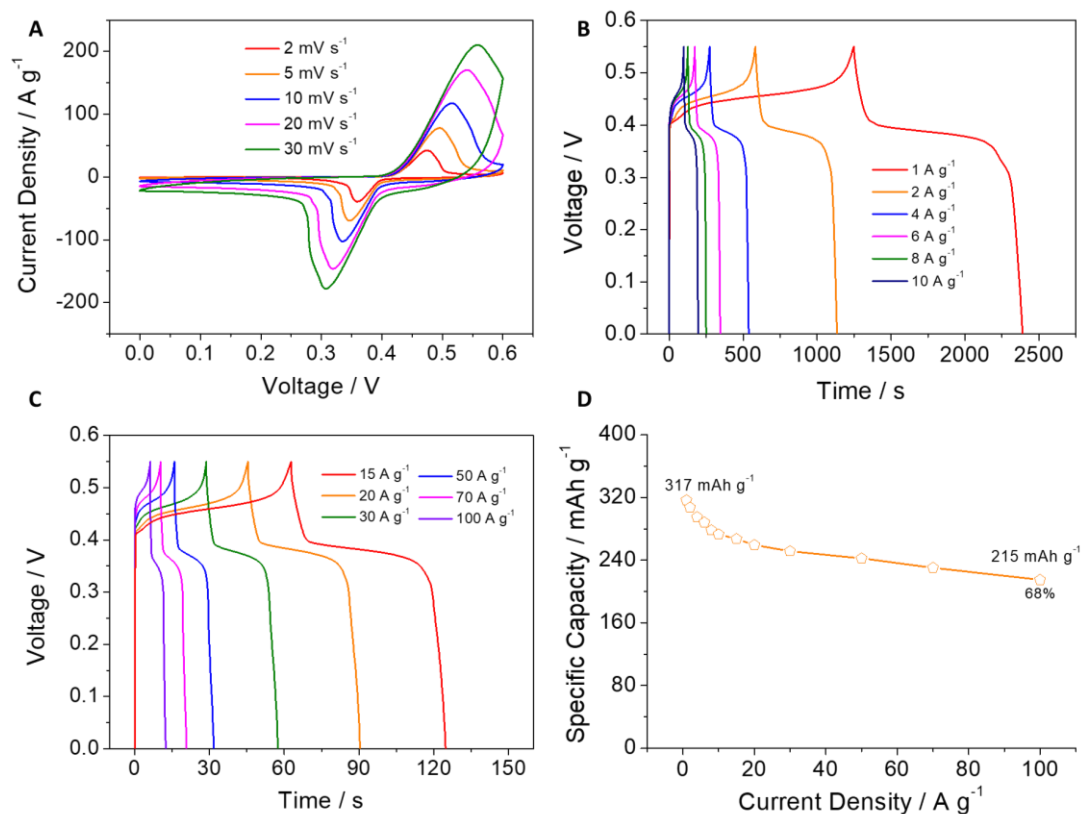
18

Figure S29. A, CV curves of the A-NiAl-LDH from 2 mV s⁻¹ to 30 mV s⁻¹. A pair of sharp redox peaks can be found at different scan rates, indicative of the battery-like charge storage process.[5] B, C, GCD curves of the A-NiAl-LDH hybrids at different current densities changing (B) from 1 A g⁻¹ to 10 A g⁻¹ and (C) from 15 A g⁻¹ to 100 A g⁻¹. D, Specific capacity of the A-NiAl-LDH at different current densities, which displays a high specific capacity of 317 mAh g⁻¹ at 1 A g⁻¹ with a high retention rate of 68% at 100 A g⁻¹.

Table S1. Lattice parameters of potassium-birnessite MnO_2 unit cell

Lattice parameter	Potassium-birnessite
a	6.561 Å
b	2.9417 Å
c	6.6398 Å
α	90°
β	115.295°
γ	90°

Table S2. A comparison of the electrochemical performance of the $AK-MnO_2$ and the results in literature

Electrode Materials	Electrolyte	Specific Capacitance	Rate Performance	Cycle Performance	Ref.
$AK-MnO_2$	1 M Na_2SO_4	**356 F g^{-1}**	**75%** **(1-50 A g^{-1})** **67%** **(1-100 A g^{-1})**	**91%** **(3000 cycles)** **84%** **(5000 cycles)**	*This work*
Reassembled $\delta-MnO_2$	1 M Na_2SO_4	306 F g^{-1}	38% (0.2-10 A g^{-1})	83% (1000 cycles)	*Nat. Commun. 2017, 8, 14559*
$MnO_2/pg-C_3N_4$	1 M KOH	348 F g^{-1}	72% (1-10 A g^{-1})	N/A	*Nano Energy 2020, 77, 105153*
$MnO_2@PPy$	1 M Na_2SO_4	276 F g^{-1}	73% (2-20 A g^{-1})	93% (1500 cycles)	*Nano Energy 2017, 35, 242-250*
0.8 $V-MnO_2$	0.5 M Na_2SO_4	190 F g^{-1}	37% (1-10 A g-1)	91% (5000 cycles)	*Adv. Funct. Mater. 2021, 2102693*
$MnO_2@WC$	1 M Na_2SO_4	177 F g^{-1}	44% (1-30 mA cm^{-2})	N/A	*Energy Environ. Sci., 2017,10, 538-545*
$\beta -MnO_2$ /Birnessite	1 M Na_2SO_4	306 F g^{-1}	74% (0.25-64 A g^{-1})	92% (3000 cycles)	*ACS Nano 2018, 12, 1033-*

1042

MnO$_2$@CNTs @3DGA	1 M Na$_2$SO$_4$	1.5 F cm^{-2}	43% (5-100 mV s^{-1})	N/A	*Adv. Funct. Mater. 2017, 27, 1701122*
HMONFs	1 M Na$_2$SO$_4$	292 F g^{-1}	49% (2.5-8 A g^{-1})	76% (3500 cycles)	*Nano Energy 2014, 4, 39-48*
Hierarchical MnO$_2$	1 M LiClO$_4$	298 F g^{-1}	58% (50-250 mV s^{-1})	85% (1000 cycles)	*ACS Nano 2013, 7, 1200-1214*
Silicon @MnO$_2$	1 M Na$_2$SO$_4$	342 F g^{-1}	48% (0.5-10 A g^{-1})	85% (2000 cycles)	*J. Mater. Chem. A, 2017, 5, 10856-10865*
MnO$_2$-C	1 M Na$_2$SO$_4$	287 F g^{-1}	78% (1-20 A g^{-1})	83.9% (10000 cycles)	*Chem. Eng. J. 2021, 417, 129186*
MnO$_2$/CNF	1 M Na$_2$SO$_4$	525 mF cm^{-2}/ 110 F g^{-1}	54% (3-30 mA cm^{-2})	N/A	*Adv. Energy Mater. 2015, 5, 1401882*
Ni$_{0.25}$Mn$_{0.75}$O @C	1 M LiCl	242.86 mF cm^{-2}	24% (1-16 mA cm^{-2})	73% (5000 cycles)	*Adv. Mater. 2017, 29, 1703463*

References

1. Guo, W., Yu, C., Li, S.F., Song, X.D., Huang, H.W., Han, X.T., Wang, Z., Liu, Z.B., Yu, J.H., Tan, X.Y., *et al.* (2019). A universal converse voltage process for triggering transition metal hybrids in situ phase restruction toward ultrahigh-rate supercapacitors. Adv. Mater. *31*, 1901241.

2. Vilas Bôas, N., Souza Junior, J.B., Varanda, L.C., Machado, S.A.S., and Calegaro, M.L. (2019). Bismuth and cerium doped cryptomelane-type manganese dioxide nanorods as bifunctional catalysts for rechargeable alkaline metal-air batteries. Appl. Catal. B: Environ. *258*, 118014.

3. Zhao, C.T., Yu, C., Zhang, M.D., Huang, H.W., Li, S.F., Han, X.T., Liu, Z.B., Yang, J., Xiao, W., Liang, J.N.*, et al.* (2017). Ultrafine MoO_2-carbon microstructures enable ultralong-life power-type sodium ion storage by enhanced pseudocapacitance. Adv. Energy Mater. *7*, 1602880.

4. Augustyn, V., Come, J., Lowe, M.A., Kim, J.W., Taberna, P.L., Tolbert, S.H., Abruna, H.D., Simon, P., and Dunn, B. (2013). High-rate electrochemical energy storage through Li^+ intercalation pseudocapacitance. Nat. Mater. *12*, 518-522.

5. Gogotsi, Y., and Penner, R.M. (2018). Energy storage in nanomaterials-capacitive, pseudocapacitive, or battery-like? ACS Nano *12*, 2081-2083.